Acta Crystallographica Section B
Structural Science
ISSN 0108-7681

Structure–property correlation over five phases and four transitions in $Pb_5Al_3F_{19}$

S. C. Abrahams,[a]* J. Ravez,[b] H. Ritter[c] and J. Ihringer[c]

[a]Physics Department, Southern Oregon University, Ashland, OR 97520, USA, [b]Institut de Chimie de la Matière Condensée de Bordeaux, Av. du Dr A. Schweitzer, F-33608 Pessac, France, and [c]Lehr- und Forschungsbereich für Röntgen- und Neutronenbeugung der Universität Tübingen, Auf der Morgenstelle 10, D-72076 Tübingen, Germany

Correspondence e-mail: sca@mind.net

Received 16 July 2002
Accepted 23 May 2003

The calorimetric and dielectric properties of $Pb_5Al_3F_{19}$ in the five phases stable under ambient pressure are correlated with structure for fuller characterization of each phase. The first-order transition between ferroelectric phase V and antiferroelectric phase IV at $T_{V,IV}$ = 260 (5) K exhibits a thermal hysteresis of 135 (5) K on heating, with a maximum atomic displacement $\Delta(xyz)_{max}$ = 1.21 (6) Å; the transition from phase IV to ferroelastic phase III at 315 (5) K is also first order but with a thermal hysteresis of 10 (5) K and $\Delta(xyz)_{max}$ = 0.92 (7) Å; that from phase III to paraelastic phase II at 360 (5) K is second order without hysteresis and has $\Delta(xyz)_{max}$ = 0.69 (4) Å; and the transition from phase II to paraelectric phase I at 670 (5) K is second or higher order, with $\Delta(xyz)_{max}$ = 0.7 (4) Å. The measured entropy change ΔS at $T_{V,IV}$ agrees well with ΔS as derived from the increased configurational energy by Stirling's approximation. For all other phase transitions, $0.5 \geq \Delta S > 0$ J mol^{-1} K^{-1} is consistent with an entropy change caused primarily by the changes in the vibrational energy. The structure of phase III is determined both by group theoretical/normal mode analysis and by consideration of the structures of phases II, IV and V reported previously; refinement is by simultaneous Rietveld analysis of the X-ray and neutron diffraction powder profiles. The structure of prototypic phase I is predicted on the basis of the atomic arrangement in phases II, III, IV and V. The introduction of 3*d* electrons into the $Pb_5Al_3F_{19}$ lattice disturbs the structural equilibrium, the addition of 0.04% Cr^{3+} causing significant changes in atomic positions and increasing $T_{IV,III}$ by ~15 K. Substitution of Al^{3+} by 20% or more Cr^{3+} eliminates the potential minima that otherwise stabilize phases IV, III and II.

1. Introduction

Many materials, some of which have major technological applications, undergo a single transition from a ferroic phase, but relatively few have been reported that undergo three or more phase transitions.[1] Structure and ferroic properties in phases V–II of $Pb_5Al_3F_{19}$ are correlated in §§2–5. The structure of phase I is predicted in §6 and the characteristics determined for each phase transition are presented in §§7–10. The total atomic displacements at each of the four phase transitions are given in §11, and a model for the multiple phase transitions in $Pb_5Al_3F_{19}$ which are unique among fluorides is

[1] A ferroic crystal may be defined as having one or more phases with at least two orientation states, in the absence of a magnetic or electric field or a mechanical stress, that can be shifted from one state to another by the application of a field or a stress or a combination (*cf.* Aizu, 1970). Ferroic properties include ferroelectricity, ferroelasticity and ferromagnetism (*cf.* Wadhawan, 2000).

Table 1
Lattice constants of $Pb_5Al_3F_{19}$ phases I–V, Z, as well as space groups and thermal stability ranges.

Lattice constants for phase I are estimated. The primitive unit cell of phase IV at 295 K used for structure refinement in the space group $P4/n$ has a = 20.1738 (4) Å, c = 7.2205 (1) Å and Z = 8 (Andriamampianina *et al.*, 1994). The smaller transformed cell, see §7.1, is also body-centered with symmetry reduced effectively to $I\bar{1}$.

Phase	I	II	III	IV	V
Measurement temperature (K)	–	370	320	295	160
a (Å)	~14.29	14.285 (7)	14.2622 (2)	14.2650 (4)	14.108 (7)
b (Å)	= a	= a	14.2800 (2)	= a	= a
c (Å)	~7.23	7.227 (3)	7.2340 (1)	7.2205 (1)	7.342 (7)
α (°)	90	90	90.00 (1)†	90	90
β (°)	90	90	90.510 (1)	90	90
γ (°)	90	90	90.00 (1)†	90	90
V (Å^3)	1476 (20)	1475 (1)	1473.3 (2)	1469.3 (1)	1461.3 (2)
Z	4	4	4	4	4
Space group, No.	$I4/mcm$, (140)	$I4/m$, (87)	$I\bar{1}$, (2)	$P4/n$, (85)	$I4cm$, (108)
Thermal stability range (K)‡	875–670	670–360	360–315	315–260	<260

† If allowed to vary, see §4, α and γ oscillate slightly around the value 90.00°. The uncertainty in each is taken as an order of magnitude greater than that in β. ‡ Ranges applicable on heating; see §§7 and 8 for thermal hysteresis.

given in §12. An independent solution of the structure of phase III on the basis of group theory and on the basis of the known structures in phases II, IV and V, followed by simultaneous refinement using the X-ray and neutron diffraction powder profiles, is given in §13. Finally, §14 demonstrates that a significant change in atomic positions is caused by replacing even minor proportions of Al in the $Pb_5Al_3F_{19}$ structure by a 3d element. The recommended IUCr nomenclature (Tolédano *et al.*, 1998) for the lowest temperature phase is

$$\text{V}\,|<260\ \text{K}|I4cm\,(108)|Z=4|\ \text{ferroelectric}|2\ \text{variants},$$

in which the transition temperature here and throughout §1 is that measured on heating. The next-highest temperature phase is

$$\text{IV}\,|315{-}260\ \text{K}|P4/n\,(85)|Z=8|\text{antiferroelectric}|2\,\text{variants}.$$

The remaining pure phase for which the structure has been reported is

$$\text{II}|670\text{-}360\ \text{K}|I4/m\,(87)|Z=4|\text{paraelastic}|2\,\text{variants}$$
$$\text{differing in elastic properties}.$$

The two other phases are

$$\text{III}|360\text{-}315\ \text{K}|I\bar{1}(2)|Z=4|\text{ferroelastic}|16\ \text{variants}$$

and

$$\text{I}|670-825\ \text{K}|I4/mcm\,(140)|Z=4|\text{non-ferroic}|\text{prototypic}$$
$$\text{paraelectric}.$$

A preliminary overview of the $Pb_5Al_3F_{19}$ phase system has been presented by Ravez & Abrahams (1998), with the thermal dependence of the lattice parameters between 397 and 50 K, as measured by Ihringer *et al.* (1994), reproduced in Figs. S1(*a–c*) of the supplemetary material. The structure derived hereunder for phase III has also been used by Bravic *et al.* (2000) in a single-crystal refinement of $Pb_5Al_{2.96}Cr_{0.04}F_{19}$, see §14.

2. Phase V of $Pb_5Al_3F_{19}$

2.1. Structural characteristics

The unit-cell dimensions and other comparable properties of $Pb_5Al_3F_{19}$ phase V|< 260 K|,[2] see Table 1, closely match those of $Pb_5Cr_3F_{19}$ at 295 K, *cf.* §12.1. The X-ray powder pattern intensity distributions are similar in both cases, with the solid solution formation of $Pb_5(Cr_{1-x}Al_x)_3F_{19}$ over the full composition range $0 \le x \le 1$ (Ravez *et al.*, 1990) providing strong indications early in this study that phase II of $Pb_5Cr_3F_{19}$ and phase V of $Pb_5Al_3F_{19}$ are likely to be isostructural, but see §14.2. The atomic coordinates of phase V at 160 K (Sarraute *et al.*, 1996) are given in Table S1[3] with views of the structure along the c and a axes in Figs. 1 and 2). The number of independent n-vertex PbF_n polyhedra and AlF_6 octahedra, with average bond distances, is noted in Table 2. The lattice constants and measurement temperatures of all $Pb_5Al_3F_{19}$ phases are given in Table 1.

The structure of each phase may be characterized by the orientation and tilts of the individual and the corner-sharing chain-forming AlF_6^{3-} octahedra, and also by the variation in PbF_n^{2-n} polyhedral types. The AlF_6^{3-} octahedral tilts in each phase, indicated in Table 2 by an extension of Glazer's (1972) classification, show no more than one of the six tilts associated with the two types of octahedra changes at any phase. Taking $d_{Pb-F} \le 3$ Å, corresponding to a minimum Pb—F bond valence of 0.07 based on Brese & O'Keefe's parameters (1991), Table 2 shows that the bond-valence sum for each PbF_n^{2-n} polyhedron noted does not differ significantly from the expected value. The bond-valence sums for all the Al^{3-} ions also agree with expectation.

The non-octahedral $F7^-$ ion in phase V occupies a distorted tetrahedron formed by two $Pb1^{2+}$ and two $Pb2^{2+}$ ions, with two Pb—F7 bonds of length 2.39 Å and two others of 2.79 Å. These Pb—F7 bond lengths correspond to bond valences of 0.38 and 0.13, respectively, giving a bond-valence sum of 1.02 at $F7^-$. If no other F^- ions were bonded to Pb^{2+}, $Pb_5Al_3F_{19}$ could belong to the class of inorganic compounds described by

[2] Following the initial use of this nomenclature in a paper by including all six information fields, Tolédano *et al.* (1998) recommend that subsequent use be restricted to two of the first three fields. The temperatures quoted above are derived from powder diffraction measurement.

[3] Tables S1–S12 present previously published atomic coordinates for phases V, IV and II, as well as the atomic coordinates for phase IV following transformation to the body-centered setting, the refined atomic coordinates of phase III in space group $P\bar{1}$ by Bravic *et al.* (2000) as transformed to $I\bar{1}$, and the atomic displacements along each axis at all four phase transitions. Fig. S1 presents thermal dependence data for $Pb_5Al_3F_{19}$; Fig. S2 presents two normal probability plots based on three pairs of phase III coordinates in space group $I\bar{1}$ and one based on the atomic coordinates of $Pb_5Al_3F_{19}$ phase V and $Pb_5Cr_3F_{19}$ phase II. All are available as supplementary data from the IUCr electronic archives (Reference BR0115). Services for accessing these data are described at the back of the journal.

Table 2
Structural characteristics of phases I, II, III, IV and V of $Pb_5Al_3F_{19}$.

Phase	I	II	III	IV	V
No. of independent positional variables	10	22	78	78	23
No. of independent PbF_n^{2-n} polyhedra	Two	Three	Five	Five	Two
No. of F in independent PbF_n^{2-n} polyhedra, for d(Pb—F) < 3 Å	n = 8 (× 2)	n = 7, 8 (× 2)	n = 6, 8, 9 (× 2), 10	n = 8 (× 3), 9 (× 2)	n = 9, 10
⟨Pb—F⟩ distance (Å)	2.61 (9),† 2.6 (3)	2.60 (11), 2.63 (18), 2.66 (12)	2.53 (11), 2.68 (20), 2.68 (24). 2.66 (20), 2.77 (20)	2.69 (3), 2.7 (3)	2.7 (2), 2.6 (3)
Bond-valence sum for Pb‡	1.75, 1.87	1.53, 1.82, 1.60	1.63, 1.58, 1.96, 1.87, 1.56	1.93, 1.61, 2.07, 1.45, 1.76	1.87, 2.61
No. of independent AlF_6^{3-} octahedra	Two	Two	Three	Five	Two
⟨Al—F⟩ distances (Å)	1.76 (5), 1.72 (7)	1.80 (2), 1.79 (2)	1.82 (8), 1.82 (26), 1.82 (19)	1.80 (5), 1.78 (4), 1.81 (4), 1.75 (3), 1.85 (4)	1.818 (5), 1.824 (1)
Bond-valence sum for Al	3.4, 3.7	3.0, 3.1	2.9, 2.9, 2.9	3.0, 3.2, 2.9, 3.4, 2.6	2.9, 2.8
Octahedral arrangement	Eclipsed chains and individual octahedra	Eclipsed chains and individual octahedra	Eclipsed chains and individual octahedra	Eclipsed chains and individual octahedra	Staggered chains and individual octahedra
Octahedral tilts§	$a^0\,a^0\,c^0$, $a^+a^+\,c^+$	$a^0\,a^0\,c^+$, $a^+a^+\,c^+$	$a^0\,a^0\,c^+$, $a^+a^+\,c^-$	$a^0\,a^0\,c^+$, $a^+a^+\,c^-$	$a^0\,a^0\,c^-$, $a^+a^+\,c^-$
Non-octahedral F^- ion(s)	F7	F8	F19 and F20	F21 and F22	F7
Shortest d(Pb—F) < 3 Å for non-octahedral F^- ions (Å)	Pb1—F7: 2.39 (10) Pb2—F7: 2.79 (10) (× 4)	Pb1—F8: 2.60 (3) Pb2—F8: 2.27 (2) Pb3—F8: 2.80 (2) (× 4)	Pb1—F20: 2.60 (3) Pb2—F19: 2.68 (3) Pb3—F19: 2.02 (3) Pb4—F20: 2.41 (3) Pb5—F19: 2.83 (2) Pb5—F20: 2.51 (2), 2.97 (2)	Pb1—F21: 2.64 (4) Pb2—F22: 2.29 (4) Pb3—F21: 2.25 (4) Pb4—F22: 2.54 (5) Pb5—F21: 2.71 (2), 2.74 (5) Pb5—F22: 2.62 (5)	Pb1—F7: 2.31 (2) Pb2—F7: 2.46 (2) (× 2)

† Standard uncertainties calculated by Bessel's method. ‡ See Brese & O'Keefe (1991). § Glazer's (1972) octahedral tilt classification.

Krivovichev & Filatov (1999) that contains O- or N-centered metal tetrahedra in which the metal atoms approximate close-packed spheres. The ionic radius for F^- is ∼0.07 Å smaller than that of O^{2-}, and hence Pb—Pb distances in Pb_4F are expected to be shorter than in Pb_4O tetrahedra. The shortest tetrahedral Pb—Pb distance in phase V is 3.65 Å, whereas 3.58 Å is reported by Mentzen & Latrach (1983) in $Pb_2O(SO_4)$, one of Krivovichev & Filatov's (1999) examples. The increased tetrahedral length in phase V because of the additional F^- ions in the n-vertex polyhedron of each independent Pb^{2+} ion, see Table 2, eliminates the possibility of class membership.

The role of the non-octahedral $F7^-$ ion has not previously been emphasized. $F7^-$ forms the shortest Pb—F bond in $Pb1F_9$ at 2.31 Å, but in $Pb2F_{10}$ the two with d(F3—Pb2) = 2.27 Å are shorter than the two non-octahedral bonds with d(F7—Pb2) = 2.46 Å, see Table 2 and Figs. 1 and 2.

2.2. Experimental evidence for ferroelectricity

2.2.1. Dielectric study. Dielectric measurements on ceramic disks over the frequency range 10^{-2}–10^6 Hz from 293 to 743 K were made by Omari *et al.* (1998). The transition from phase V|< 260 K| to phase IV|315–260 K| could not be studied by impedance spectroscopy because of the increasing resistance in $Pb_5Al_3F_{19}$ samples below room temperature, but the transitions from phase IV to phase III|360–315 K| and from phase III to phase II|670–360 K| are readily observed. Analysis by complex permittivity formalism allows both isochronous and isothermal values of $\varepsilon'(f,T)$ and $\varepsilon''(f,T)$, where ε' is the real and ε'' the imaginary dielectric permittivity, to be determined as a function of frequency (f) and temperature (T). Significant perturbations are indiscernable at the lower-temperature phase transitions, but a major maximum in ε' is detectable isochronously at $T \simeq 670$ K for $f \geq 10^5$ Hz. This reproducible dielectric anomaly is reversible and corresponds to the transition from paraelastic phase II to the previously undetected prototypic paraelectric phase I|> 670 K| with the probable space group $I4/mcm$. $T_{I,II}$ is not frequency dependent, and hence this transition is not of the relaxor type (Ishchuk, 2001).

2.2.2. Piezoelectric and pyroelectric properties. Piezoelectric resonances produced in $Pb_5Al_3F_{19}$ phase V|< 260 K| crystals under the application of frequencies ranging from kHz to MHz are readily detected; analysis of the characteristic reciprocal impedance demonstrates the formation of a typical piezoelectric compression mode at ∼1197 kHz (Sarraute *et al.*, 1996). The mechanical quality factor $Q_m(Pb_5Al_3F_{19}) = 1/2\pi RCf_r \simeq 423$ (where R is the resistance, C the capacitance and f_r the resonance frequency) is comparable to that of $Q_m(BaTiO_3) \simeq 300$ and $Q_m(PbZr_{0.45}Ti_{0.55}O_3) \simeq 543$. Unambiguous detection of piezoelectricity is a necessary condition

to prove the absence of inversion centers but is insufficient *per se* to prove the presence of ferroelectricity, see *e.g.* Abrahams (1994).

Pyroelectric measurements on phase V are readily made by rapidly varying the temperature of a $Pb_5Al_3F_{19}$ crystal with (001) faces connected to an electrometer. The pyroelectric coefficient $p_3 \simeq 20\,\mu C\,m^{-2}\,K^{-1}$ determined by thermal pulsing (Sarraute *et al.*, 1996) confirms the presence of a polar axis; this observation is also a necessary but not a sufficient condition to prove the existence of ferroelectricity.

2.2.3. Conductivity, band gap and hysteresis test. The conductivity, $\sigma \simeq 10^{-24}\,S\,m^{-1}$, of $Pb_5Al_3F_{19}$ is very low at $T_{V,IV} < 260$ (5) K. From 293 to 360 K, however, $\log \sigma T$ varies linearly with $1/T$ and corresponds to a band gap of 0.63 eV (Omari *et al.*, 1998). The classical dielectric hysteresis test for the presence of ferroelectricity is inapplicable, despite the low conductivity, owing to electrical breakdown at fields higher than $\sim$0.7 MV m^{-1} that prevents the application of fields greater than the coercive value E_C.[4]

2.2.4. Calorimetry and ^{19}F NMR spectra. The heat capacity of $Pb_5Al_3F_{19}$ between 190 and 690 K was measured with a Perkin Elmer DSC-7 differential scanning calorimeter. The results, shown in Fig. 11, are highly reproducible between 255 and 382 K; variations much outside this range are undiscernible and hence omitted. The changes in heat capacity measured at each transition are discussed below.

The temperature dependence of the F^- ion mobility determined from ^{19}F NMR spectra varies smoothly on the NMR time-scale from $\sim$2.5% in phase V to $\sim$91% in phase IV, with an inflection at $T_{V,IV}$ as the spectral linewidth decreases from $\sim$60 to $\sim$10 kHz (Omari *et al.*, 1998).

2.3. Structural basis for ferroelectricity

Sarraute *et al.* (1996) noted that the polar z coordinate of each atom in $Pb_5Al_3F_{19}$ at 160 K is within 0.83 Å of that required to achieve centrosymmetry in space group *I*4/*mcm* and also that each Δz_i magnitude exceeds the corresponding static/thermal displacement u_i except for Δz(F5) $\simeq u$(F5). The largest $\Delta\xi$ displacements in Table S1 are 0.97 Å for Δx(F1), Δy(F1) and 0.89 Å for Δx(F2), Δy(F2). The structural criteria for ferroelectricity (Abrahams, 1988) are hence fully satisfied by phase V and, together with the major maximum in dielectric permittivity in ε' detectable isochronously at 670 (5) K in §2.2.1 and the calculated value of $T_c \simeq 860$ (230) K in §2.3.1, the property may be taken to be satisfactorily confirmed.[5]

2.3.1. Calculation of T_c and P_s. The largest polar displacement by an Al atom in phase V at 160 K from a location with zero polarization is $\Delta z = 0.204$ (8) Å (Table S1). The corresponding predicted Curie temperature, T_c, from

$$T_c = (\kappa/2k)(\Delta z)^2\ \text{K}, \qquad (1)$$

is 835 (65) K, where $\kappa \simeq 5.52$ kPa is a force constant, k is Boltzmann's constant and $\kappa/2k = 2.00\,(9) \times 10^4$ K Å^{-2} (Abrahams *et al.*, 1968). The uncertainty estimate in T_c neglects the component due to F-atom positions determined by X-ray diffraction in the presence of Pb.

The magnitude of the spontaneous polarization, P_s, at 160 K may be derived from (2), using the atomic coordinates in Table S1 and a point charge model:

$$P_s = (e/V)\sum Z_j \Delta z_j. \qquad (2)$$

Summing over the unit-cell volume V, with charge Z^j (2+ for Pb, 3+ for Al and 1− for F) on the jth ion and displacement Δz_j, gives $P_s = 2.2\,(3) \times 10^{-2}$ C m^{-2}.[6] This P_s value in phase V, with its general atomic distribution, agrees well with that expected for three-dimensional ferroelectrics in which $P_s \leq 3 \times 10^{-2}$ C m^{-2} (Abrahams & Keve, 1971*a*).

2.4. Structural correlation with ferroelectricity

Relationship (1) assumes the Curie temperature is coincident with the ferroelectric to-paraelectric phase transition. It is notable that the estimated value of T_c is so close to the transition temperature $T_{II,I} \simeq 670$ K, in view of the three intervening phases between the ferroelectric phase V and the prototypic phase I in $Pb_5Al_3F_{19}$. The implication follows that the critical Δz, and hence P_s, has attained a maximum magnitude in phase V at the structure determination temperature of 160 K. Factors contributing to the stability of the intervening $Pb_5Al_3F_{19}$ phases are discussed in §12.

3. Phase IV of $Pb_5Al_3F_{19}$

3.1. Structural characteristics

The structure of phase IV|315–260 K| (Andriamampianina *et al.*, 1994), unlike phase V |< 260 K|, contains infinite chains of *eclipsed* corner-sharing AlF_6 octahedra as well as individual octahedra. The arrangement and number of octahedra, PbF_n polyhedra and non-octahedral F^- ions, as well as the averaged bond distances $d\langle$Pb—F$\rangle$ and $d\langle$Al—F$\rangle$, are summarized in Table 2. The atomic coordinates given in Table S2 are transformed to the setting and orientation of phase V in Table S3 for direct comparison, see §7.1, with a view of the structure in Figs. 3 and 4. The non-octahedral F21$^-$ and F22$^-$ ions in phase IV form the shortest bond lengths in the $Pb2F_8$, $Pb3F_8$ and $Pb4F_8$ polyhedra but, in the $Pb1F_9$ polyhedron, d(Pb1—F21) = 2.64 Å, with four shorter octahedral F^- bonds of length 2.36–2.51 Å. In the $Pb5F_9$ polyhedron, F21$^-$ forms two bonds with $d \simeq 2.72$ Å, while d(Pb5—F22$^-$) = 2.62 Å and there are four shorter octahedral F^- bonds of length 2.48–2.60 Å, see Table 2 and Figs. 3 and 4. The non-octahedral F^- ions in phases IV and V, *cf.* §2.1, hence have comparable roles.

[4] Electric fields required for polarization saturation run as high as 100 MV m^{-1} (*e.g.* Wang *et al.*, 2003).

[5] Ferroic materials that are unable to complete a ferroic transition because of decomposition or other causes form the basis for Wadhawan's (2000) definition, 'A ferroic material is one that can, or can be conceived to, undergo one or more ferroic phase transitions'.

[6] The SI units for P_s are mC m^{-2}, but the customary units used are as given above.

3.2. Experimental evidence for antiferroelectricity

A double *P*–*E* hysteresis loop formed by inducing a polarization (*P*) at high field strength (*E*), with the transition temperature close to that of a maximum in $\varepsilon'(f,T)$, would provide unambiguous evidence for antiferroelectricity. The combination of a high coercive field and a low breakdown strength in phase IV prevents such observations. Measurement of the permittivity temperature dependence under an applied electric field similarly proved to be impractical. The conductivity leads to frequency dispersion in ε', with relaxation at $T > 260$ K, but the electric modulus frequency dependence increases by an order of magnitude at $T_{IV,III}$, *cf.* §8.

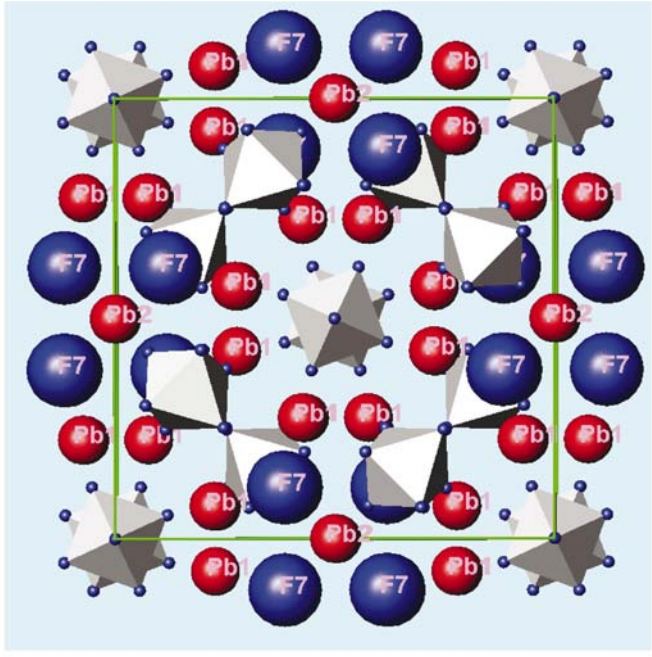

Figure 1
Figs. 1–10 show views of the structure of all five $Pb_5Al_3F_{19}$ phases at ambient pressure. Non-octahedral ions are labelled, with Pb^{2+} presented in red and F^- in blue. The AlF_6 octahedra are presented in silver. Shannon's radii are used, except for the octahedral F^- ions. Ferroelectric phase V structure at 160 K, along the *c* axis.

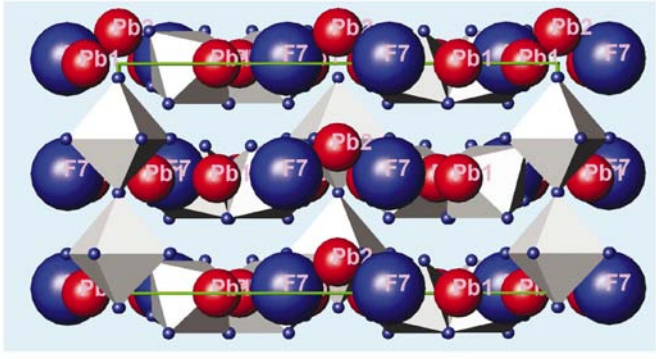

Figure 2
Ferroelectric phase V structure at 160 K, along the *a* axis.

3.3. Structural basis for antiferroelectricity

Distortions from regularity in the five independent AlF_6 octahedra of phase IV result in the development of appreciable electric dipoles. However, each dipole formed in this phase is cancelled by an equal but opposite dipole as a consequence of the 4/*m* point-group symmetry. The structural requirement for antiferroelectricity, in which all polarization components along the unique axis cancel, is hence satisfied.

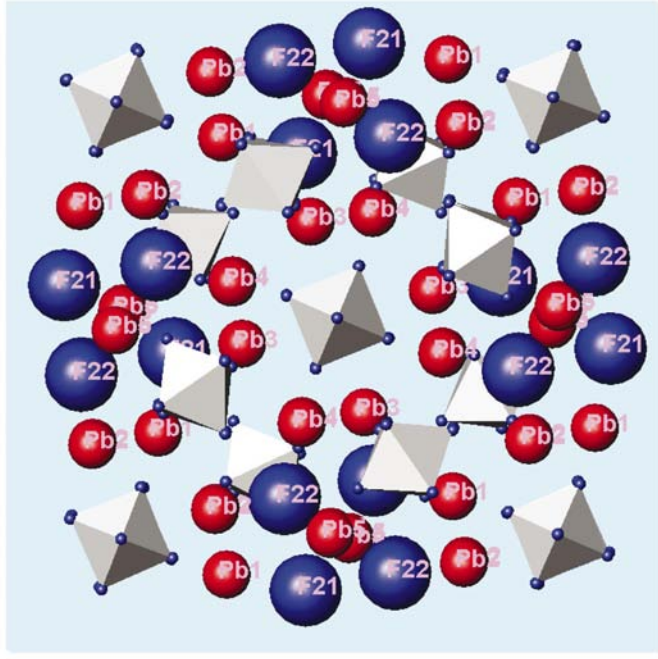

Figure 3
Antiferroelectric phase IV structure at 295 K, along the *c* axis.

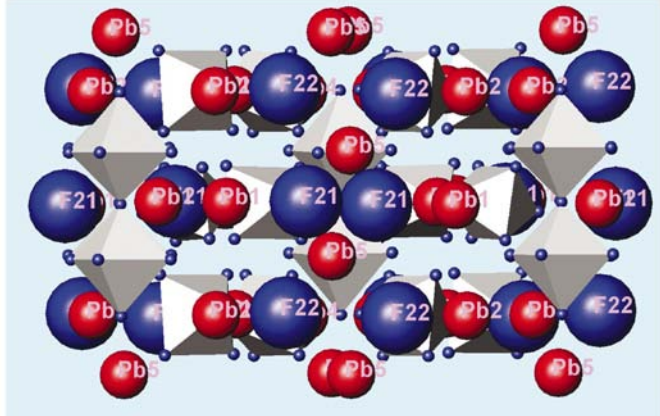

Figure 4
Antiferroelectric phase IV structure at 295 K, along the *a* axis.

4. Phase III of $Pb_5Al_3F_{19}$

4.1. Symmetry of ferroelastic phase III

The thermal dependence study of the $Pb_5Al_3F_{19}$ lattice parameters shows that the unit cell remains body-centered on cooling from phase II|670–360 K| as the β angle increases abruptly from 90° at $T_{II,III}$, reaching a maximum of ∼90.5° at $T_{III,IV}$ without discernable departure of either the α or the γ angle from 90°, see Fig. S1 and Table 1 (Ihringer *et al.*, 1994). The possibility that the symmetry in phase III might be monoclinic may be discarded since the twofold axis in phase III is normal to and hence underivable from the fourfold axis in phase II with its twofold axis approximately parallel to $\mathbf{a}_2$, and the fourfold axis to **c**. In addition, the AlF_6 octahedra in adjacent phases II and IV are ferrorotatively twisted ∼22° about **c** from a position that would fit a monoclinic lattice with the *b* axis unique. For the structure of phase III to be a subgroup of *I*4/*m* (phase II) and *I*4/*mcm* (phase I), the observed symmetry is best fit by the space group $I\bar{1}$.

The β-angle thermal dependence in Figs. S1(*b*) and (*d*) indicates a transformation within phase III, over which the powder diffraction profile changes continuously. Analysis of the symmetry changes resulting from mode softening in space group *I*4/*mcm* (phase I), deduction of the structure from the $Pb_5Al_3F_{19}$ phases already determined, and the results of Rietveld analysis with structural refinement are given in §13.

4.2. Structural characteristics

The distribution and arrangement of independent PbF_n^{2-n} polyhedra, AlF_6^{3-} octahedra and non-octahedral F^- ions in phase III are summarized in Table 2, together with the bond-valence sums and averaged bond distances. Corner-sharing eclipsed AlF_6 octahedra form infinite chains similar to those in phase IV. The averaged bond length $d\langle Al-F\rangle$ = 1.82 (2) Å in each octahedron agrees well with the value of 1.825 Å derived from Shannon's (1976) ionic radii. A view of the structure in phase III along the *c* axis is shown in Fig. 5 and along the *a* axis in Fig. 6. The non-octahedral $F19^-$ and $F20^-$ ions in phase III have roles comparable to that in phases V and IV, see §§2.1 and 3.1. With five independent Pb polyhedra in phase III, the shortest Pb—F(non-octahedral) bond forms in $Pb3F_9$ and $Pb4F_9$, with d(F19—Pb3) = 2.19 Å and d(F20—Pb4) = 2.35 Å (see Table 3). In $Pb1F_6$, however, three octahedral F^- bonds of length 2.37–2.52 Å are shorter than d(F20—Pb1) = 2.58 Å; in $Pb2F_8$, $F19^-$ forms a bond with d = 2.51 Å, but d(F8—Pb2) = 2.35 Å; in $Pb5F_{10}$, d(F20—Pb5) = 2.58 and 2.99 Å, d(F19—Pb5) = 2.98 Å, but an octahedral F^- bond is shorter at d(F10—Pb5) = 2.50 Å.

4.3. Experimental evidence for ferroelasticity

Phase III|360–315 K| undergoes a first-order transition on heating from phase IV with a thermal hysteresis of 10 (5) K [Ravez *et al.* (1994) report ∼20 K]. Twin domains are invariably produced in the ferroelastic phase, either at the transition on heating phase IV or at that on cooling from phase II. Domain walls in thin crystals are clearly visible under a polarizing microscope throughout the thermal phase-stability range, mostly oriented along [001] but with some normal to **c**. The latter form a small minority and appear to originate at crystal defects caused by internal stress, disappearing sharply at the transition to phase II. In contrast, the domains disappear more gradually at the transition to phase IV; distinct regions of phase IV often form and coexist within the crystalline phase III over a thermal range of ∼ 20 K on cooling. Commonly, one region is domain free (assumed to be phase IV), while the domain walls are readily observed in other regions (assumed to be phase III). Two-phase coexistence provides unambiguous evidence of a first-order phase transition. Domain walls in a ferroelastic crystal may generally be moved and even eliminated to yield a detwinned crystal by the

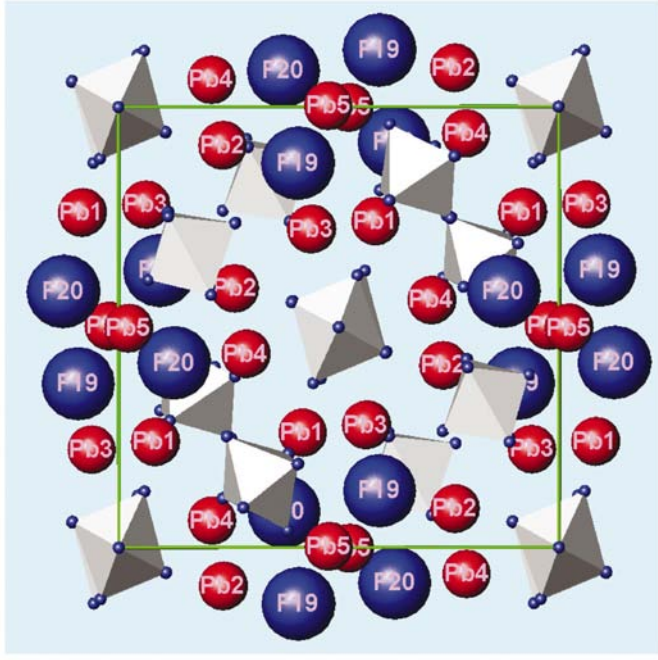

Figure 5
Ferroelastic phase III structure at 320 K, along the *c* axis with the *b* axis horizontal.

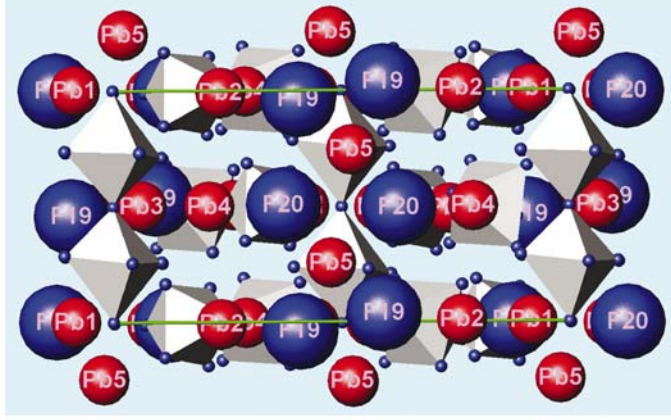

Figure 6
Ferroelastic phase III structure at 320 K, along the *a* axis.

Table 3
Coordination distances (Å) in $Pb_5Al_3F_{19}$ phase III at 320 (2) K.

Pb1—F11^{i}	2.37 (3)	Pb3—F17^{iii}	2.86 (4)
Pb1—F1^{i}	2.43 (3)	Pb3—F18^{iii}	2.99 (3)
Pb1—F16^{ii}	2.52 (3)		
Pb1—F7	2.58 (3)	Pb4—F20^{ii}	2.35 (3)
Pb1—F20^{ii}	2.63 (3)	Pb4—F5^{i}	2.46 (3)
Pb1—F15^{i}	2.63 (3)	Pb4—F6^{i}	2.48 (3)
		Pb4—F2^{ii}	2.58 (3)
Pb2—F8^{ii}	2.35 (3)	Pb4—F17	2.72 (3)
Pb2—F19^{i}	2.51 (3)	Pb4—F11^{i}	2.76 (3)
Pb2—F12^{ii}	2.56 (2)	Pb4—F8	2.83 (3)
Pb2—F5^{iii}	2.71 (3)	Pb4—F18^{iii}	2.85 (4)
Pb2—F18^{i}	2.73 (4)	Pb4—F16	2.90 (4)
Pb2—F9^{i}	2.78 (3)		
Pb2—F17^{ii}	2.79 (3)	Pb5—F10^{i}	2.50 (3)
Pb2—F3	2.99 (4)	Pb5—F9	2.57 (3)
		Pb5—F20^{ii}	2.58 (3)
Pb3—F19^{i}	2.19 (3)	Pb5—F9	2.61 (3)
Pb3—F12^{ii}	2.49 (3)	Pb5—F10^{ii}	2.62 (3)
Pb3—F4^{i}	2.56 (3)	Pb5—F19	2.91 (4)
Pb3—F3^{i}	2.61 (3)	Pb5—F7	2.92 (3)
Pb3—F15	2.74 (3)	Pb5—F5^{i}	2.98 (3)
Pb3—F16	2.77 (4)	Pb5—F19	2.98 (4)
Pb3—F7^{ii}	2.85 (3)	Pb5—F20^{ii}	2.99 (3)
Al1—F1^{i}	1.78 (3)	Al2—F3^{ii}	1.81 (4)
Al1—F2^{ii}	1.71 (4)	Al2—F4^{i}	1.60 (4)
Al1—F6^{i}	1.80 (3)	Al2—F5	2.01 (4)
Al1—F7	1.90 (3)	Al2—F8^{i}	2.12 (4)
Al1—F9	1.87 (4)	Al2—F10	1.94 (3)
Al1—F11	1.83 (4)	Al2—F12	1.43 (3)
Al3—F13	1.85 (3)	Al3—F16	2.14 (4)
Al3—F14	1.78 (3)	Al3—F17^{iii}	1.89 (4)
Al3—F15	1.66 (4)	Al3—F18^{iii}	1.61 (4)

Symmetry codes: (i) $\frac{1}{2}-x,\frac{1}{2}-y,\frac{1}{2}-z$; (ii) $\frac{1}{2}+x,\frac{1}{2}+y,\frac{1}{2}+z$; (iii) $-x,-y,-z$.

application of stress along an appropriate direction, see *e.g.* Abrahams (1994); it has not been possible to grow crystals of phase III with mechanical strength sufficient to withstand the requisite compressive stress.

4.4. Calculation of spontaneous strain $\mathbf{e_s}$ and ferroelastic atomic displacements

The transition from phase IV to phase III is accompanied by dimensional and angular distortions of the unit cell, giving rise to different ferroelastic spontaneous strains. The equivalence of a_1 and a_2 in tetragonal $I4/m$ is replaced by inequivalent a and b axes in triclinic $I\bar{1}$. The resulting spontaneous strain-tensor component is given by $e_{12} = [(a-b)\sin\gamma]/2a_T$, where the b-axis direction is common to both phases and the subscript refers to the tetragonal phase. Assuming $\gamma \simeq 89.97^\circ$, *i.e.* differs from 90° by 3σ in phase III, then $|e_{12}| \simeq 6.48 \times 10^{-4}$ at 320 K, see Table 1. Since the b axis is longer than the a axis, the application of compressive stress along [010] is expected to result in axial interchange and spontaneous strain reorientation. In the second category, the tetragonal base vectors become distorted to give a temperature-dependent β angle (~90.5° at 320 K) and $|e_{13}| = \frac{1}{2}(a\sin\gamma\cos\beta^*/a_T - c\sin\alpha\cos\beta^*/c_T) \simeq 1.23 \times 10^{-3}$. The application of compressive stress along [101] is expected to reorient **a** or **c**, thereby changing β to $180^\circ - \beta$.

The angles α and γ in the triclinic unit cell are deformable ferroelastically from $90^\circ + \delta_i$ to $90^\circ - \delta_i$, where $i = 1$ or 3. The temperature dependence of α and γ and the magnitude of the coercive stress required to achieve either form of ferroelastic reorientation has not yet been determined.

All ferroelastic crystals contain pseudosymmetrically related pairs of atoms with coordinates

$$(x_1y_1z_1) = f(x_2y_2z_2) + \Delta\xi, \qquad (3)$$

where $f(x_2y_2z_2)$ is a transformation that causes the reorientation of the lattice vectors under applied stress and $\Delta\xi$ is the displacement between resulting atomic positions; the latter generally have maximum magnitudes of the order of 1 Å (see *e.g.* Abrahams, 1994). Equation (3) is applicable to the tetragonal symmetry of both phases I and II, with relationships

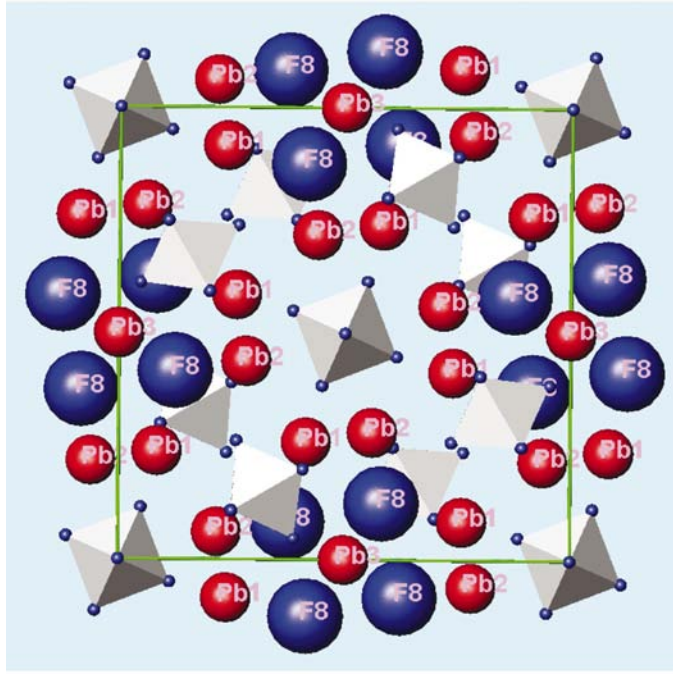

Figure 7
Paraelastic phase II structure at 370 K, along the *c* axis.

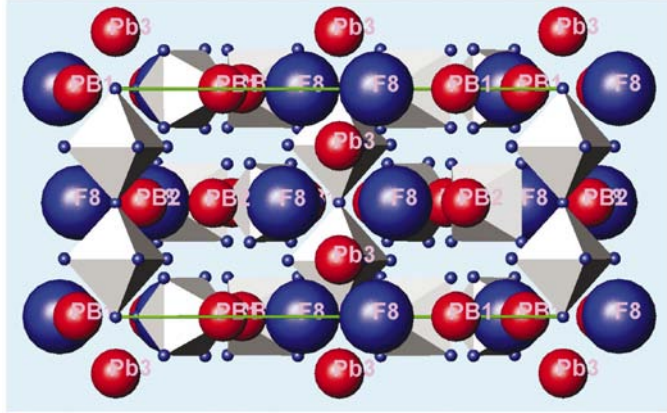

Figure 8
Paraelastic phase II structure at 370 K, along the *a* axis.

Table 4
Equivalent coordinate values for all atoms in $Pb_5Al_3F_{19}$ phases V, IV and II, with refined and expected coordinates [Av(excluding III)] and uncertainties ($\bar{\sigma}$) in phase III and in phase I [Av(all)].

Wyckoff positions in non-standard centered cells are denoted by primes. The coordinates of F1[a], F3[h], F4[c], F6[g] and F7[a] in phase V are the symmetry equivalents of those given by Sarraute *et al.* (1996), see transformations below. Expressions such as Pb1 ⇒ 1 indicate a coordinate transformation from that given in Tables 1S, 3S and 5 and in the CIF to that of a corresponding atom in phase V.

Phase	Wyckoff position	Atom	*x*	*y*	*z*
V	16(*d*)	Pb1	0.4260	0.2749	0
IV	4′(*g*)	Pb1 ⇒ 1[a]	0.4133	0.2601	0.0091
	4′(*g*)	Pb2 ⇒ 1[b]	0.4361	0.2843	0.0037
	4′(*g*)	Pb3 ⇒ 1[c]	0.4411	0.2811	0.0007
	4′(*g*)	Pb4 ⇒ 1[d]	0.4160	0.2604	−0.0042
III	4′(*e*)	Pb1 ⇒ 1[a]	0.4174	0.2603	0.0038
	4′(*e*)	Pb2 ⇒ 1[e]	0.4124	0.2633	−0.0080
	4′(*e*)	Pb3 ⇒ 1[f]	0.4377	0.2778	−0.0033
	4′(*e*)	Pb4 ⇒ 1[c]	0.4390	0.2891	0.0001
II	8(*h*)	Pb1 ⇒ 1[d]	0.4153	0.2603	0
	8(*h*)	Pb2 ⇒ 1[g]	0.4388	0.2823	0
Av(all)†		Pb1	0.4266	0.2722	0.000
		$\overline{\sigma}$(Pb1)	0.012	0.011	0.005
Av(excluding III)		Pb1	0.4267	0.2719	0.001
		$\overline{\sigma}$(Pb1)	0.012	0.011	0.004
V	4(*b*)	Pb2	0	1/2	0.1350
IV	4′(*g*)	Pb5 ⇒ 2[h]	0.0210	0.4926	0.2352
III	4′(*e*)	Pb5 ⇒ 2[-]	0.0023	0.4772	0.2557
II	4(*d*)	Pb3 ⇒ 2[-]	0	1/2	1/4
Av(all)		Pb2	0.006	0.493	0.22
		$\overline{\sigma}$(Pb2)	0.010	0.011	0.03
Av(excluding III)		Pb2	0.007	0.4975	0.21
		$\overline{\sigma}$(Pb2)	0.016	0.004	0.06
V	8(*c*)	Al1	0.1628	0.3372	−0.021
IV	4′(*g*)	Al4 ⇒ 1[e]	0.1735	0.3409	0.0054
	4′(*g*)	Al5 ⇒ 1[i]	0.1558	0.3248	−0.0079
III	4′(*e*)	Al1 ⇒ 1[-]	0.1519	0.3193	−0.010
	4′(*e*)	Al2 ⇒ 1[j]	0.1925	0.3265	0.021
II	8(*h*)	Al1	0.1581	0.3255	0
Av(all)		Al1	0.166	0.329	−0.002
		$\overline{\sigma}$(Al1)	0.007	0.011	0.003
Av(excluding III)		Al1	0.1626	0.332	−0.006
		$\overline{\sigma}$(Al1)	0.008	0.008	0.004
V	4(*a*)	Al2	0	0	0.188
IV	1′(*c*)	Al1 ⇒ 2[g]	0	0	0.2389
	1′(*c*)	Al2 ⇒ 2[d]	0	0	0.2580
	2′(*f*)	Al3 ⇒ 2[f]	0	0	0.2437
III	4′(*e*)	Al3 ⇒ 2[-]	0.0044	0.0128	0.245
II	4(*e*)	Al2	0	0	0.2460
Av(all)		Al2	0.001	0.002	0.2366
		$\overline{\sigma}$(Al2)	0.0020	0.006	0.0018
Av(excluding III)		Al2	0	0	0.235
		$\overline{\sigma}$(Al2)	0	0	0.025
V	16(*d*)	F1	0.2478	0.1140	0.326
IV	4′(*g*)	F9 ⇒ 1[d]	0.2587	0.1023	0.3438
	4′(*g*)	F10 ⇒ 1[b]	0.3126	0.0892	0.3415
	4′(*g*)	F16 ⇒ 1[g]	0.3031	0.0893	0.3154
	4′(*g*)	F19 ⇒ 1[k]	0.2576	0.0944	0.3176
III	4′(*e*)	F2 ⇒ 1[l]	0.2363	0.1116	0.339
	4′(*e*)	F3 ⇒ 1[d]	0.2394	0.1116	0.349
	4′(*e*)	F4 ⇒ 1[j]	0.2481	0.1133	0.333
	4′(*e*)	F6 ⇒ 1[m]	0.2835	0.0908	0.305
II	16(*i*)	F5‡ ⇒ 1	0.2506	0.1079	0.3300
Av(all)		F1	0.264	0.102	0.330
		$\overline{\sigma}$(F1)	0.030	0.010	0.011
Av(excluding III)		F1	0.272	0.099	0.329
		$\overline{\sigma}$(F1)	0.011	0.010	0.012
V	16(*d*)	F2	0.1970	0.4294	0.142
IV	4′(*g*)	F11 ⇒ 2[f]	0.2030	0.4080	0.1578
	4′(*g*)	F12 ⇒ 2[e]	0.2595	0.3733	0.1682
	4′(*g*)	F17 ⇒ 2[i]	0.2148	0.4004	0.1774
	4′(*g*)	F18 ⇒ 2[l]	0.2562	0.3902	0.1731

such as $\frac{1}{2}-y, \frac{1}{2}+x, \frac{1}{2}+z$ in phase I; several forms of (3) are symmetry equivalent. The resulting relations

$$(x_1, y_1, z_1) = (-y_2, x_2, z_2) + \Delta\xi_j, \qquad (4)$$

$$(x, y, z) = [x(1 + 2z \sin\delta_i), y, z] + \Delta\xi_j \qquad (5)$$

allow the $\Delta\xi$ magnitudes to be derived from related pairs of atomic coordinates (see CIF.) The maximum values of $\Delta\xi_j$ from (4) are 0.46 Å for Pb5/Pb5′, 0.38 Å for Al1/Al2′ and 0.76 Å for F6/F3′, where the prime indicates transformed coordinates. The base vector triplet **a**, **b**, **c** is hence transformable to the triplet −**b**, **a**, **c** under the application of appropriately oriented tensile or compressive stress, whereas (5) is consistent with a change in β angle from $90^\circ + \delta_2$ to $90^\circ - \delta_2$. Comparable relationships may be derived for changes in α and γ.

5. Phase II of $Pb_5Al_3F_{19}$

5.1. Structural characteristics

The atomic coordinates of the paraelastic phase II|670–360 K| determined by Sarraute *et al.* (1995) are presented in Table S4, with a view of the structure shown in Figs. 7 and 8. A summary of the polyhedral and octahedral arrangement, and also the averaged Al—F and Pb—F distances including non-octahedral $F8^-$ ions bonded to Pb^{2+}, is given in Table 2. The only polyhedron in phase II in which the shortest Pb—F bond is formed by the non-octahedral $F8^-$ ion is $Pb2F_8$, in which d(F8—Pb2) = 2.27 Å. In the $Pb1F_7$ polyhedron, however, three octahedral F^- bonds of length 2.52–2.54 Å are shorter than d(F8—Pb1) = 2.60 Å, while $F8^-$ in the $Pb3F_8$ polyhedron forms four bonds with d = 2.80 Å, but four shorter octahedral F^- bonds of length 2.51 Å.

5.2. Structural correlation with paraelasticity

The property of paraelasticity is appropriately ascribed to a phase that, on cooling, develops ferroelasticity without the concurrent development of additional ferroic properties, as in the transition from phase II to phase III. The atomic arrangement in the centrosymmetric phase II, with two elastic domains, is also consistent with the property of paraelectricity, but since ferroelectricity does not develop at the transition to phase III the paraelectric description is more apposite for prototypic phase I, see §9.

Table 4 (continued)

Phase	Wyckoff position	Atom	x	y	z
III	4′(*e*)	F1 ⇒ 2^c	0.2122	0.3855	0.181
	4′(*e*)	F5 ⇒ 2^n	0.2107	0.4265	0.149
	4′(*e*)	F7 ⇒ 2^-	0.1895	0.4066	0.175
	4′(*e*)	F8 ⇒ 2^o	0.2063	0.4088	0.187
II	16(*i*)	F4 ⇒ 2^-	0.2001	0.4076	0.1730
Av(all)		F2	0.215	0.404	0.168
		$\overline{\sigma}$(F2)	0.024	0.017	0.014
Av(excluding III)		F2	0.2218	0.4015	0.1653
		$\overline{\sigma}$(F2)	0.028	0.014	0.013
V	8(*c*)	F3^v	−0.0761	0.4239	0.403
IV	4′(*g*)	F14 ⇒ 3^i	−0.1127	0.4487	0.5434
	4′(*g*)	F15 ⇒ 3^o	−0.1101	0.4561	0.5062
III	4′(*e*)	F9 ⇒ 3^h	−0.0391	0.3837	0.456
	4′(*e*)	F10 ⇒ 3^k	−0.0683	0.3922	0.493
II	8(*h*)	F7 ⇒ 3^b	−0.1120	0.4456	1/2
Av(all)		F3	−0.086	0.425	0.484
		$\overline{\sigma}$(F3)	0.030	0.050	0.048
Av(excluding III)		F3	−0.103	0.444	0.488
		$\overline{\sigma}$(F3)	0.018	0.014	0.060
V	8(*c*)	F4	0.2521	0.2479	0.569
IV	4′(*g*)	F13 ⇒ 4^b	0.2364	0.2402	0.4837
	4′(*g*)	F20 ⇒ 4^g	0.2383	0.2409	0.4546
III	4′(*e*)	F11 ⇒ 4^a	0.2541	0.2524	0.555
	4′(*e*)	F12 ⇒ 4^h	0.2643	0.2641	0.515
II	8(*h*)	F6 ⇒ 4^c	0.2370	0.2390	1/2
Av(all)		F4	0.247	0.247	0.513
		$\overline{\sigma}$(F4)	0.012	0.010	0.043
Av(excluding III)		F4	0.2410	0.2420	0.502
		$\overline{\sigma}$(F4)	0.008	0.004	0.049
V	4(*a*)	F5	0	0	0.438
IV	1′(*c*),1′(*c*), 1′(*a*),1′(*b*)	F1,2,5,8 ⇒ $5^{l,g,-,e}$	0	0	1/2
III	2′(*b*)	F13 ⇒ 5	0	0	1/2
	2′(*a*)	F14 ⇒ 5^e	0	0	1/2
II	2(*b*)	F1,2 ⇒ $5^{e,-,e}$	0	0	1/2
Av(all)		F5	0	0	1/2
		$\overline{\sigma}$(F5)	0	0	0
Av(excluding III)		F5	0	0	1/2
		$\overline{\sigma}$(F5)	0	0	0
V	16(*d*)	F6^g	0.4460	0.6175	0.173
IV	4′(*g*)	F3 ⇒ 6^e	0.3836	0.5464	0.2322
	4′(*g*)	F4 ⇒ 6^b	0.4487	0.6131	0.2553
	4′(*g*)	F6 ⇒ 6^c	0.4495	0.6163	0.2232
	4′(*g*)	F7 ⇒ 6^g	0.4490	0.6152	0.2329
III	4′(*e*)	F15 ⇒ 6^d	0.3829	0.5421	0.254
	4′(*e*)	F16 ⇒ 6^j	0.3727	0.5583	0.270
	4′(*e*)	F17 ⇒ 6^g	0.4435	0.6069	0.211
	4′(*e*)	F18 ⇒ 6^c	0.4412	0.6055	0.239
II	16(*i*)	F3 ⇒ 6^n	0.4500	0.6146	0.2460
Av(all)		F6	0.427	0.594	0.234
		$\overline{\sigma}$(F6)	0.026	0.031	0.027
Av(excluding III)		F6	0.4378	0.6039	0.227
		$\overline{\sigma}$(F6)	0.03	0.03	0.029
V	8(*c*)	F7^c	0.1165	0.3835	0.521
IV	4′(*g*)	F21 ⇒ 7^i	0.0793	0.3753	0.4904
	4′(*g*)	F22 ⇒ 7^e	0.1254	0.4126	0.5122
III	4′(*e*)	F19 ⇒ 7^e	0.1284	0.4073	0.537
	4′(*e*)	F20 ⇒ 3^k	0.1257	0.4189	0.505
II	8(*h*)	F8^c ⇒ 7^c	0.0830	0.3750	1/2
Av(all)		F7	0.110	0.395	0.511
		$\overline{\sigma}$(F7)	0.021	0.020	0.017
Av(excluding III)		F7	0.1011	0.3866	0.506
		$\overline{\sigma}$(F7)	0.023	0.018	0.013

The transformation coordinates, from the space group *I*4*cm*, are (*a*) $y, x, \frac{1}{2}+z$; (*b*) $\bar{y}, x, z$; (*c*) $\frac{1}{2}-x, \frac{1}{2}-y, \frac{1}{2}+z$; (*d*) $\frac{1}{2}-x, \frac{1}{2}+y, z$; (*e*) $x, \bar{y}, \frac{1}{2}+z$; (*f*) $\frac{1}{2}+y, \frac{1}{2}-x, \frac{1}{2}+z$; (*g*) $\frac{1}{2}+x, \frac{1}{2}+y, \frac{1}{2}+z$; (*h*) $\bar{x}, y, \frac{1}{2}+z$; (*i*) $\bar{x}, \bar{y}, z$; (*j*) $\frac{1}{2}+x, \frac{1}{2}-y, z$; (*k*) $\bar{y}, \bar{x}, \frac{1}{2}+z$; (*l*) $\frac{1}{2}+y, \frac{1}{2}+x, z$; (*m*) $\frac{1}{2}-y, \frac{1}{2}-x, z$; (*n*) $y, \bar{x}, z$; (*o*) $\frac{1}{2}-y, \frac{1}{2}+x, \frac{1}{2}+z$. A hyphen represents the identity x, y, z. † Av(all) presents the mean over each coordinate in phases V, IV, III and II; Av(excluding III) presents the mean over each coordinate only in phases V, IV and II. Means close to special positions are assumed to occupy such positions in phase I. The standard mean uncertainties $\bar{\sigma}$ were calculated from Bessel's formula. ‡ See the footnote to Table 4S for the transformation of F5, phase II, within the space group *I*4/*m*.

6. Phase I of $Pb_5Al_3F_{19}$

Assuming the space group of $Pb_5Al_3F_{19}$ in the paraelectric phase I is a supergroup to phases V, IV, III and II then it is most likely to be *I*4/*mcm*, *i.e.* identical to that predicted for paraelectric $Pb_5Cr_3F_{19}$ (Abrahams *et al.*, 1990). Phase I melts incongruently at 825 (5) K, the thermal stability limit (Andriamampianina, 1992).

6.1. Structural characteristics

The atomic coordinates predicted in the prototype structure are taken as the average of those determined in phases V, IV and II together with the refined atomic coordinates of the ferroelastic phase III, as listed under 'Av(All)' in Table 4. Full determination of the structure in phase I awaits measurement.

The predicted atomic coordinates for phase I in Table 5 correspond to a unit cell containing two independent PbF_8 polyhedra, two AlF_6 octahedra and the non-octahedral $F7^-$ ion as noted in Table 2. The resulting bond distances in Table 6 are necessarily approximate but are in agreement with the more accurate values determined in the four other phases. A view of the predicted structure is given in Figs. 9 and 10. The shortest Pb—F bond in the $Pb1F_8$ polyhedron is formed by the non-octahedral $F7^-$ ion with d(F7—Pb1) = 2.4 Å. In the $Pb2F_8$ polyhedron, however, four octahedral F^- ions form bonds of length 2.4 Å, which are shorter than those formed by the four non-octahedral F^- ions, with d(F7—Pb2) = 2.8 Å. The role of the non-octahedral ion in phase I is hence comparable with that in the four other phases.

7. Phase V to phase IV transition in $Pb_5Al_3F_{19}$

The transition in $Pb_5Al_3F_{19}$ from the ferroelectric phase V|< 270 K| *I*4*cm* to the antiferroelectric phase IV in *P*4/*n* approaches first order, thermodynamically, with a thermal hysteresis of 135 (5) K (*cf.* ∼130 K; Ravez *et al.*, 1994), the coexistence of phases V and IV over ∼15 K and an abrupt change of ∼1.9% in unit-cell dimensions, see Fig. S1 (Ihringer *et al.*, 1994). The entropy change ΔS measured calorimetrically at $T_{V,IV}$ is 11.9 J mol^{-1} K^{-1} on heating and 16.5 J mol^{-1} K^{-1} on cooling, with an endotherm 3 K wide at half height. Part of ΔS at $T_{V,IV}$ is because of the abrupt change from a staggered arrangement of AlF_6 octahedra along the rotation-tetrad axes in phase V to an eclipsed arrangement along the corresponding inversion and rotation-tetrad axes in phase IV, *cf.* Figs. 1 and 2, and 3 and 4. Taking the primary contribution to the entropy change at $T_{V,IV}$ as the change in configurational thermal

Table 5
Predicted atomic coordinates in phase I.

Averaged over coordinate values derived in space group *I*4/*mcm* from experimental values determined in phases II, III, IV and V. Atomic numbering as in phase V, except F1, which is the mean of the Av(all)F1 and Av(all)F2 coordinate values in Table 4. The standard uncertainties are from Table 4.

Phase I	Wyckoff position	*x*	*y*	*z*
Pb1†	16(*k*)	0.427 (12)	0.272 (11)	0
Pb2	4(*b*)	0	1/2	1/4
Al1	8(*h*)	0.168 (7)	0.332	0
Al2	4(*a*)	0	0	1/4
F1	32(*m*)	0.274 (29)	0.099 (10)	0.331 (11)
F3	8(*h*)	−0.081 (30)	0.419	1/2
F4	8(*h*)	0.250 (11)	0.250	1/2
F5	4(*c*)	0	0	1/2
F6	16(*i*)	0.417 (33)	0.583	1/4
F7‡	8(*h*)	0.107 (21)	0.393	1/2

† Coordinates from Table 4 adjusted to meet the required symmetry of all but the 32(*m*) Wyckoff site. ‡ The non-octahedral F^- ion.

energy corresponding to the increase from 23 to 78 independent position parameters (see Table 2), Stirling's approximation gives $\Delta S \simeq R\ln(78/23) = 10.2\ \mathrm{J\ mol^{-1}\ K^{-1}}$, in good agreement with experiment.

7.1. Atomic displacements at $T_{V,IV}$

Atomic displacements between phases V and IV are not subject to group–subgroup relations and are determined here from differences between coordinates of comparable atoms in the two phases (Tables S1 and S2/S3). The calculation of these differences, as with those between phases IV and III, is facilitated by the transformation to a body-centered unit cell for phase IV, see Table 1. The original $x'y'z'$ coordinates in a primitive unit cell with $a' = 20.1738$ Å, $c' = 7.2205$ Å and space group *P*4/*n* in Table S2 are transformed by (6) to the set of *xyz* atomic coordinates in Table S3, the symmetry of the resulting body-centered array with $a = a'(2)^{1/2} = 14.2650$ Å and $c = c' = 7.2205$ Å reducing in effect to the space group $I\bar{1}$:

$$x = x' + y';\ y = -x' + y' + \frac{1}{2};\ z = z' + \frac{1}{2}. \qquad (6)$$

The translation along *b* is caused by the change in origin from a fourfold axis to an inversion center. Comparable atomic coordinates in each phase are presented in Table 4, after minimizing $\Sigma[z_V - 1/n\Sigma(|z_{IV-II}|)]$ for each of the *n* variable *z* coordinates in phases IV to II with respect to the independent atoms in phase V.

The largest total displacement ($\Delta\xi$) at the transition from phase V to phase IV in Table S5 is 1.21 Å, by an F2 atom in the atomic numbering of phase V, with six other atoms displaced between 1.20 and 0.86 Å and seven more by $\Delta\xi \geq 0.5$ Å. The largest Pb^{2+} displacement at the phase transition is 0.79 Å, by Pb2. Displacements by all atoms in $Pb_5Al_3F_{19}$ at each phase transition are considered in §11.

Table 6
Coordination distances (Å) in the predicted structure of phase I of $Pb_5Al_3F_{19}$ (Table 5).

Pb1—F7^{i}	2.41†	Pb2—F3	2.43 × 4
Pb1—F1^{ii}	2.50 × 2	Pb2—F7^{vii}	2.82 × 4
Pb1—F4^{i}	2.55		
Pb1—F6^{iii}	2.75 × 2		
Pb1—F1^{iv}	2.83 × 2		
Al1—F4^{i}	1.66	Al2—F6^{viii}	1.68 × 4
Al1—F3^{v}	1.76	Al2—F5	1.81 × 2
Al1—F1^{vi}	1.78 × 4		

Symmetry codes: (i) $\frac{1}{2}-x, x, 0$; (ii) $\frac{1}{2}-y, \frac{1}{2}-x, z$; (iii) $x, x, \frac{1}{4}$; (iv) $\frac{1}{2}+y, \frac{1}{2}-x, \frac{1}{2}-z$; (v) $\bar{x}, \frac{1}{2}-x, 0$; (vi) $\frac{1}{2}-x, \frac{1}{2}-y, \frac{1}{2}-z$; (vii) $x, \frac{1}{2}-x, \frac{1}{2}$; (viii) $\frac{1}{2}-x, \frac{1}{2}-x, \frac{1}{4}$. † Standard mean uncertainties from Table 4: ∼0.3 Å in *d*(Pb—F), ∼0.5 Å in *d*(Al—F).

8. Phase IV to phase III transition in $Pb_5Al_3F_{19}$

The continuity in lattice spacing variation through the phase transition at $T_{IV,III}$ is in sharp contrast to the major disconti-

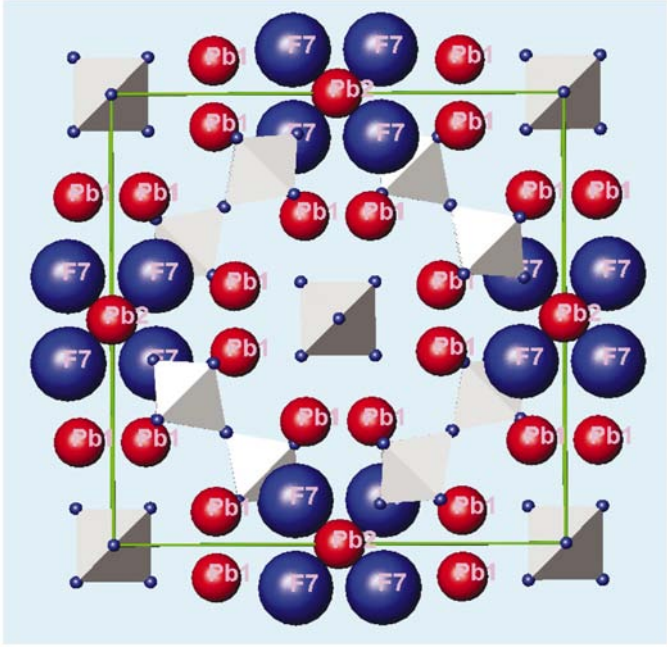

Figure 9
Predicted (670–825 K) paraelectric phase I structure, along the *c* axis.

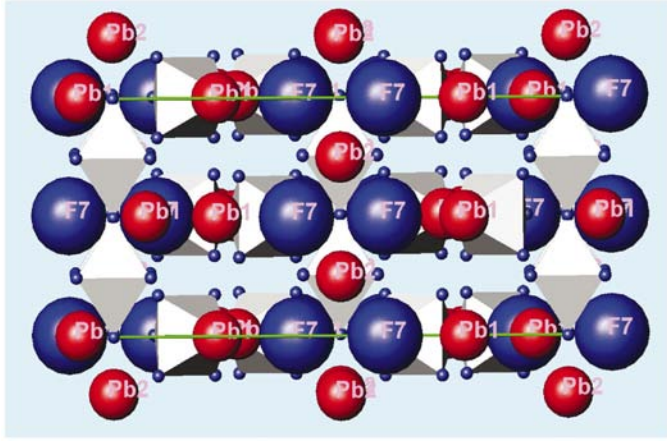

Figure 10
Predicted (670–825 K) paraelectric phase I structure, along the *a* axis.

Table 7
Total atomic displacement ($\Delta\xi$, Å) at the transitions between phases V and IV; IV and III; III and II; and II and I.

Based on averaged lattice constants from Table 1 and atomic displacement components in Tables 5S, 6S, 7S and 8S, with designations as in Table 4.

Atom No. in Phase V	Phase V/IV	Phase IV/III	Phase III/II	Phase II/I
Pb1	0.34	0.07	0.04	0.24
	0.30	0.10	0.08	0.22
	0.34	0.12	0.07	
	0.38	0.07	0.10	
Pb2	0.79	0.53	0.33	0
Al1	0.25	0.49	0.14	0.17
	0.22	0.10	0.37	
Al2	0.37	0.20	0.19	0.03
	0.51	0.21		
	0.41	0.19		
F1	0.26	0.35	0.22	0.38
	0.99	0.49	0.47	
	0.86	0.87	0.09	
	0.32	0.42	0.59	
F2	0.34	0.23	0.12	0.38
	1.21	0.92	0.25	
	0.55	0.23	0.29	
	1.03	0.85	0.19	
F3	1.20	0.63	0.42	0.66
	1.00	0.35	0.12	
F4	0.67	0.57	0.34	0.24
	0.86	0.76	0.31	
F5	0.45 × 4	0 × 4	0 × 2	0 × 2
F6	0.44	0.17	0.22	0.65
	0.60	0.25	0.22	
	0.37	0.23	0.09	
	0.44	0.21	0.56	
F7†	0.59	0.12	0.69	0.43
	0.44	0.20	0.58	

† Non-octahedral F^- ion.

nuity exhibited by the thermally dependent β angle, see Figs. S1(*a*) and (*b*). The wide thermal range (~20 K) over which phases III|360–315 K| and IV|315–260 K| coexist, together with a thermal hysteresis of 10 (5) K at $T_{IV,III}$, are clear indications of a first-order phase transition, *cf.* §7.

The calorimetric entropy change ΔS at $T_{IV,III} \simeq 0.5$ J mol^{-1} K^{-1} is less than that observed at the $T_{V,IV}$ transition by over an order of magnitude, see Fig. 2. The number of independent positional variables in phase III is 78, identical to that in phase IV. The positive entropy change is hence unrelated to a change in configurational energy; it is more likely attributable to an increase in vibrational energy, in view of the 44% increase in $\langle u_{iso(Pb + Al)}\rangle$, see Table S2 and the CIF. The transition at $T_{IV,III}$ results in a major change in the frequency of the maximum in electric modulus M'' from ~560 Hz at 313 K to ~3160 Hz at 328 K (M'' is the imaginary part of $M^* = 1/\varepsilon^*$, the inverse permittivity), see also §2.2.1.

8.1. Atomic displacements at $T_{IV,III}$

The total and corresponding axial components of the displacements between atomic coordinates in phase IV at 295 K and those in phase III at 320 K, see Table S3 and the CIF, are presented in Table S6. The largest total atomic displacement, $\Delta\xi_{max} = 0.92$ Å, is for F8, in the atomic numbering of phase III, with five other $\Delta\xi \geq 0.5$ Å. Magnitudes of $\Delta\xi$ at all four phase transitions are considered in §11.

9. Phase III/phase II transition in $Pb_5Al_3F_{19}$

The lack of thermal hysteresis or phase coexistence at $T_{III,II}$ together with the unit-cell volume continuity and group–subgroup relationship between phases III (point group $\bar{1}$) and II (point group 4/*m*) is indicative of a second- or higher-order transition. The measured change in entropy $\Delta S \simeq 0.5$ J mol^{-1} K^{-1} at $T_{III,II}$ is accompanied by a decrease from 78 independent positional parameters in the triclinic phase III to 22 in the tetragonal phase II, see Table S4. As in the transition at $T_{IV,III}$, that at $T_{III,II}$ cannot be associated with an increase in configurational energy. The 22% increase in $\langle u_{iso(all\ atoms)}\rangle$ indicates that the primary contribution to ΔS is an increase in vibrational energy, see Tables S2 and S4. Fig. 11 notably reveals a near-continuous increase in entropy between ~328 and 345 K; the determination and analysis of a possible change in the X-ray diffuse scattering background at $T \geq T_{III,II}$ may be revealing, but is beyond the scope of this investigation.

The stability range of phase III is dependent on grain size and/or internal strain, leading to the possibility of variation among samples. At 358 K, the electric modulus, M'', reaches a maximum at ~5 kHz, see §8, the frequency undergoing a major change on passing through $T_{III,II}$ as it increases to ~125 kHz at 383 K, see also §2.2.1.

9.1. Atomic displacements at $T_{II,III}$

The axial components and the total magnitude of each atomic displacement at $T_{III,II}$ are given in Table S7 and the total displacement magnitude of each atom at each of the four phase transitions is given in Table 7. With $\Delta\xi_{max} = 0.69$ Å (F8 in phase II designation) and only two other $\Delta\xi \geq 0.5$ Å, all displacement magnitudes at $T_{III,II}$ are significantly reduced

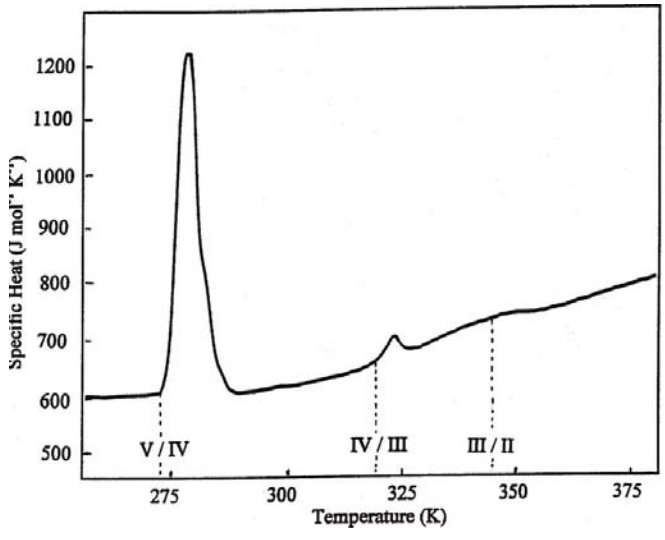

Figure 11
Thermal dependence, on heating, of the heat capacity in $Pb_5Al_3F_{19}$ between 255 and 382 K, with the phase-transition onset temperatures shown as dotted lines.

compared with those at $T_{V,IV}$ and $T_{IV,III}$, see Table 7. The corresponding atom numbering among all phases is given in Table 4.

10. Phase II/phase I transition in $Pb_5Al_3F_{19}$

A major dielectric permittivity maximum is readily detectable at $T_{II,I} \simeq 670$ K, although neither thermal hysteresis nor specific heat anomaly is observed despite minor fluctuations in heat capacity, with $\Delta S << 0.4$ J mol^{-1} K^{-1}. The order of the phase transition is hence likely to be second or higher. The 382–690 K range is omitted from Fig. 11 since fluctuations at $T_{II,I}$ are indiscernable on the scale used. The number of positional parameters at $T_{II,I}$ decreases, from 22 to 10, as it does at $T_{III,II}$, suggesting the primary contribution to the entropy increase is again in the vibrational energy.

The four transitions in $Pb_5Al_3F_{19}$ contrast strikingly with the single phase transition in the $Pb_5M_3F_{19}$ family, for M = Ti, V, Cr, Fe and Ga; see §12. It is notable that the measured range of Curie temperatures in $Pb_5M_3F_{19}$ ($545 \leq T_c \leq 740$ K) includes $T_{II,I} \simeq 670$ K in $Pb_5Al_3F_{19}$. The isochronous permittivity maximum at $T_{II,I}$ in $Pb_5Al_3F_{19}$, readily observable at frequencies of the order of 0.1 MHz (see §2.2.1), is comparable with the dielectric permittivity peak in $Pb_5Ti_3F_{19}$ at 695 K and 1 kHz (Ravez *et al.*, 1991).

10.1. Atomic displacements at $T_{II,I}$

The axial components of atomic displacement at $T_{II,I}$, based on the structure of phase II in Table S4 and that predicted for phase I in Table 5, are given in Table S8; the total displacement of each atom at each phase transition is given in Table 7. The largest component displacements at $T_{II,I}$ are ~0.5 Å by x(F3) and x(F6), and ~0.4 Å by y(F3) and y(F6) in phase I designation. All atoms with variable coordinates except Al2 have $\Delta\xi > u_{eq}$ at $T_{II,I}$; displacements at $T_{II,I}$ are comparable to those at $T_{III,II}$, but significantly smaller than at the lower-temperature phase transitions. Since the coordinates for phase I are averaged over the values determined in the four other phases, the displacements in Table S8 are necessarily open to bias.

11. Total atomic displacements at the phase transitions

Landau's (1937) theory is applicable to a wide range of structural phase transitions on the basis of macroscopic physical and microscopic atomic property measurements in the thermal range approaching T_c (*cf.* Tolédano & Tolédano, 1987). Mechanical, optical, electrical, magnetic, elastic and thermal data fall within the category of applicable macroscopic properties, while the microscopic category includes atomic displacements, symmetry, normal modes and spin configurations. Atomic displacements over a multiple series of phase transitions are not usually available, hence their magnitudes are emphasized in this study with a view to their possible future application.

The total $\Delta\xi$ displacement magnitudes for all atoms at each of the four phase transitions in $Pb_5Al_3F_{19}$ are given in Table 7, their axial components in Tables S5–S8. Atomic positions at the measurement temperatures are assumed to be identical to those at temperatures closer to each transition, although significant residual shifts are possible as a transition is approached, hence the actual displacements may differ slightly from those in Table 7.

Five independent F atoms have characteristic displacement magnitudes at $T_{V,IV}$ of $1.2 \geq \Delta\xi \geq 1$ Å, with $0.9 \geq \Delta\xi \geq 0.4$ Å for 12 others including Pb2 at $\Delta\xi = 0.79$ Å in phase V designation. The large F atom displacements at $T_{V,IV}$ are due to the abrupt onset of the AlF_6 octahedral rotations noted in §7. The entropy change at the transition between phase V and phase IV is correspondingly large at $R\ln 7 \geq \Delta S \geq R\ln 4$, see §7. Atoms F1, F2 and F4 undergo displacements at $T_{IV,III}$ of $0.9 \geq \Delta\xi \geq 0.8$ Å, eight others having $0.6 \geq \Delta\xi(F) \geq 0.4$ Å with $\Delta\xi$(Pb2), $\Delta\xi$(Al1) $\simeq 0.5$ Å. F7 has the largest $\Delta\xi$ at $T_{III,II}$ of 0.7 Å, six others having $\Delta\xi(F) \geq 0.4$ Å; $\Delta\xi$(Pb2) = 0.33 Å. At $T_{II,I}$, the atoms F3 and F6 have $0.7 > \Delta\xi > 0.6$ Å with all the remaining $\Delta\xi \leq 0.4$ Å.

The maximum $\Delta\xi$ displacements in Table 7 at any $Pb_5Al_3F_{19}$ phase transition are ~0.8 Å by Pb, ~0.5 Å by Al and ~1.2 Å by F. These magnitudes support an increased upper limit for $\Delta\xi$ at a structurally predicted ferroelectric phase transition, taken as 1.0 Å for the Δz component since the initial suggestion by Abrahams (1979, 1988).[7]

12. Multiple phase transition model for $Pb_5Al_3F_{19}$

The five $Pb_5Al_3F_{19}$ phases that form in the temperature range below 825 K reduce to two, isostructural with phases V and I, on replacing Al by M = Ti, V, Cr, Fe or Ga (Ravez *et al.*, 1991), see §12.1. The suppression of phases IV, III and II has two likely causes, an ionic radius mismatch with the interstitial spaces between PbF_n polyhedra caused by the presence of octahedral ions larger than Al^{3+} (0.675 Å), as is the case throughout the range 0.810 Å for Ti^{3+} to 0.755 Å for Cr^{3+} (Shannon, 1976), and/or the 3*d* electrons associated with the five latter ions. The low-tolerance ionic radius mismatch possibility may be tested by replacing Pb^{2+} with Ba^{2+} (radius ~0.12 Å larger than Pb^{2+} for all the coordination numbers, CN, in Table 2), thereby increasing the space available for M^{3+} ions. $Ba_5Al_3F_{19}$ is metastable at room temperature. On replacing Al^{3+} by Ga^{3+} (radius 0.76 Å) to give isotypic $Ba_5Ga_3F_{19}$, only two phases form, with $T_c(Ba_5Ga_3F_{19}) \simeq$ 1070 K; the increase in interstitial space due to Ba^{2+} relative to that in $Pb_5Al_3F_{19}$ exceeds the increase owing to Ga^{3+} in $Ba_5Ga_3F_{19}$, indicating that ionic size is not critical. It may be noted that, of 16 known members in the $A_5M_3F_{19}$ family with A = Pb, Ba or Sr, only $Pb_5Al_3F_{19}$ forms five phases (Ravez *et al.*, 1991). All other stable members contain 3*d* electrons and form only two phases. The two less likely causes of phase suppression are the $6(sp)^2$ lone electron pair and the non-

[7] The hypothetical atomic displacement magnitudes, $\Delta\xi_i$, at the experimental temperature T (160 K for phase V, $Pb_5Al_3F_{19}$), required for a ferroelectric crystal to achieve paraelectric symmetry at T_c (see *e.g.* Table S1), may differ from but tend towards the actual displacement magnitudes of corresponding *i*th atoms at the phase transition as $T \rightarrow T_c$.

Table 8
Irreducible representations at Γ in space group *I*4/*mcm* for the atoms of each orbit.

Irreducible representation of *I*4/*mcm*	Orbit							Resulting space group	
	4*a*	4*b*	4*c*	8*h*	16*i*	16*k*	32 *m*		
A_{1g}		1		1	1	2	3	*I*4/*mcm*	
A_{2g}	1			1	2	2	3	*I*4/*m*11	*I*4/*m*
B_{1g}				1	2	2	3	*I*2/*m*2/*c*1	*Ibam*
B_{2g}				1	1	2	3	*I*2/*m*12/*m*	*Fmmm*
E_g^{11}; E_g^{22}	1; 1	1; 1		1; 1	3; 3	2 ; 2	6 ; 6	*I*12/*c*1	*I*2/*c*
A_{1u}			1		1	1	3	*I*422	
A_{2u}	1	1	1	1	2	1	3	*I*4*cm*	
B_{1u}				1	2	1	3	*I*$\bar{4}$2*m*	
B_{2u}					1	1	3	*I*$\bar{4}$*c*2	
E_u^{11}; E_u^{22}	1; 1	1; 1	2; 2	2; 2	3; 3	4; 4	6; 6	*Imc*2	

octahedral F^- ions; the latter are common to all family members, the former to all with *A* = Pb, and hence neither is likely to have more than a secondary influence on the number of stable phases formed.

In addition to the presence of systematic differences between the structure of $Pb_5Al_3F_{19}$ in phase V and that of $Pb_5Cr_3F_{19}$ in phase II, see §14.2, the mean-square thermal/static atomic displacement parameters in the two structures also differ systematically. The averaged amplitudes $\bar{U}_{iso}$(Pb) = 0.015 (2) Å^2, $\bar{U}_{iso}$(Al) = 0.008 (3) Å^2 and $\bar{U}_{eq}$(F) = 0.016 (5) Å^2 in $Pb_5Al_3F_{19}$ phase V are significantly smaller than $\bar{U}_{eq}$(Pb) = 0.031 (18) Å^2, $\bar{U}_{eq}$(Cr) = 0.011 (4) Å^2 and $\bar{U}_{eq}$(F) = 0.041 (19) Å^2 in $Pb_5Cr_3F_{19}$ phase II, see Tables S1 and S12. Averaged over all atoms, $\bar{U}$ ($Pb_5Al_3F_{19}$ phase V) = 0.015 Å^2 and $\bar{U}$ ($Pb_5Cr_3F_{19}$ phase II) = 0.036 Å^2.

The global increase in $\bar{U}_{eq}$ ($Pb_5Cr_3F_{19}$ phase II) by a factor of more than 2 corresponds to an increase in thermal energy that suggests a model in which the three 3*d* Cr^{3+} ion electrons contribute to the destabilization of minima in the free-energy surfaces of $Pb_5Al_3F_{19}$ phases IV, III and II The low atomic displacement parameters in $Pb_5Al_3F_{19}$ phase V are consistent with the ^{19}F NMR investigation, see §2.2.4, in which the F^- ions are shown to be largely immobile below 190 K, rising to ∼50% mobility at 270 K and to ∼90% mobility above 360 K. In the absence of 3*d* electrons, three new phases in $Pb_5Al_3F_{19}$ become stable in succession as the temperature of phase V is raised. All three phases are eliminated if Al is replaced by more than ∼20% of a 3*d* element (Ravez *et al.*, 1994). The thermal dependence of phase II as a function of Cr^{3+} concentration has not been investigated but, as it rises above ∼15%, phase IV is suppressed followed by phase III at concentration levels $c_{Cr} \geq 20\%$. Phase V is stable at all 3*d* element concentrations, as is phase I. The structural sensitivity to replacement of Al^{3+} by as little as 0.04% Cr^{3+} is marked by an increase of ∼15 K in $T_{IV,III}$. The model presented is hence consistent with all observations.

12.1. Comparative properties of $Pb_5Cr_3F_{19}$

The two phases of $Pb_5Cr_3F_{19}$, phase II|$\lesssim$ 545 K|*I*4*cm* (108)|*Z* = 4|ferroelectric|2 variants, with *a* = 14.384 (5) Å and *c* = 7.408 (2) Å at 295 K, and phase I|$\gtrsim$ 545 K|*I*4/*mcm* (140)|*Z* = 4|non-ferroic|paraelectric, are separated by a *single* first-order transition at T_c (Arquis-Canouet *et al.*, 1986; Abrahams *et al.*, 1990). The lattice parameters undergo sharp discontinuities of 0.58% in *a* and −0.57% in *c* at T_c = 545 K, with phase coexistence over the range $T_c \pm 5$ K. Calorimetrically, ΔS = 13 (3) J mol^{-1} K^{-1}. The decreased number of positional parameters above the phase transition suggests the primary contribution to the entropy increase is a change in vibrational energy. A maximum in $\varepsilon'(f,T)$, see §2.2.1, coincides with T_c. The paraelectric Curie–Weiss behavior at $T > T_c$ is that expected for a classical ferroelectric, with T_c frequency independent. An experimental structural determination of phase I is awaited.

13. Structure of $Pb_5Al_3F_{19}$ phase III by group theory, from phases V, IV and II, and by X-ray and neutron powder diffraction profile analysis

Initially, the symmetry of phase III appeared monoclinic, but structural considerations strongly indicated the space group is $I\bar{1}$, see §4.1. The latter symmetry was independently confirmed by analysis of the atomic displacements caused by normal modes acting on the atomic arrangement in the prototype phase. Following the procedure of Landau & Lifschitz (1971), as developed by Ihringer & Abrahams (1984), see also Aroyo & Perez-Mato (1998), if the temperature-dependent atomic displacements close to a phase transition are small, then they may be regarded as equivalent to disturbances in the free energy, *G*. Consideration of the lowest-order displacements by means of a Taylor-series expansion in *G* then provides a simple thermodynamic model for such a phase transition. Since *G* is invariant under all symmetry operations of the higher-temperature space group, all terms containing atomic shifts must similarly be invariant at the critical temperature T_c. It is computationally convenient to separate each atomic displacement into a vector, **e**, giving the direction of the displacement field for all atoms involved in the transition, and a scalar quantity, η, which is the order parameter.

13.1. Selection of active irreducible representations from the change in crystal system

Displacements of the lower symmetry couple to strain tensor components and can cause lattice constants to change at a phase transition. The measurement of such change provides an indication of the collective atomic displacement directions on analysis of the atomic positions. It is evident from the thermal expansion that the atoms have moved under A_{1g} symmetry, see §4.1. The thermal dependence of the variation in the β angle follows a critical power law (Ihringer *et al.*, 1994), hence the strain tensor $2e_{12}$ may be assumed to result in a linear coupling between the change in β and the order parameter.

Free-energy invariance with respect to any coordinate transformation corresponds to a polynomial of symmetry-invariant products between the strain and order parameter components only. A linear coupling between these parameters, however, is invariant if both transform according to the same irreducible representation. Since the tensor component e_{13} in the tetragonal crystal system transforms as the irreducible representation E_g (see *e.g.* Ihringer & Abrahams, 1984), it may be expected that the order parameter is an E_g representation of $I4/mcm$.

The change in the crystal system from tetragonal to triclinic changes the atomic position coordinate system. Even without atomic coordinate change, all atoms in the tetragonal cell become displaced with E_g symmetry as the axial lengths change with temperature. Since atomic displacements with E_g symmetry are produced in the transitions to phase III from either phase IV|315–260 K| or phase II|670–360 K|, see §13.3, E_g displacements must be considered.

All the possible structures resulting from one or more phase transitions, together with their active representations, may be determined in principle from the isotropy subgroup tables for the 230 space groups (Stokes & Hatch, 1988). The determination above that one of the active degrees of freedom is a displacement with E_g symmetry (see also §13.2) allows the following discussion to be appreciably shortened.

Table 8 shows that displacements with E_g symmetry result in the space group $I12/c1$, and those with B_{2g} symmetry in the space group $I2/m12/m$, see §13.3. A single base vector of irreducible representation E_g combines with a displacement of B_{2g} symmetry to yield triclinic space group $I\bar{1}$. This space group also results from a combination of two base vectors of irreducible representation E_g, with an arbitrary phase; the results in §13.3, however, demonstrate that the $I\bar{1}$ data refine best for the combination of E_g and B_{2g} symmetry.

13.2. Group theoretical/normal mode analysis of the transition from phase II to phase III

Differences between atomic positions in the structure of phase II|670–360 K| and phase IV|315–260 K| may be taken as the sum of the normal mode displacements expressed by the atomic degrees of freedom in phase II. This sum may be assumed to contain the modes that cause the atomic shifts leading to the structure of phase III. Each mode exhibits one symmetry-adapted degree of freedom. The possibility of a phase transition from phase II to phase IV was hence investigated by the normal mode concept outlined in §13. The evaluation of normal mode coordinate displacements in the higher-symmetry space group is straightforward if the structures in the two phases are known. In that case, the N basis vectors $\mathbf{e}_k^{j\mu}$ for all irreducible representations j with multiplicity m^j ($\mu = 1,...,m^j$) and dimensions d^j ($k = 1,...,d^j$) may be taken as forming an orthonormal basis for any $3N$-dimensional vector, $\Delta\mathbf{x}$, of a given orbit, see Table 8. The $\Delta\mathbf{x}$ vectors applied to atomic shifts contain the displacements in all three coordinates for each of the N atoms in the orbit. Hence, $\Delta\mathbf{x}$ is a linear combination of $\mathbf{e}_k^{j\mu}$,

$$\Delta\mathbf{x} = \sum_j \sum_\mu \sum_k a_k^{j\mu} \cdot \mathbf{e}_k^{j\mu}. \quad (7)$$

Since $\mathbf{e}_k^{j\mu}$ are orthogonal and normalized to unity, the coefficients for each basis vector k in the representation $j\mu$ are given by the product of (7) and $\mathbf{e}_k^{j\mu}$,

$$a_k^{j\mu} = \Delta\mathbf{x} \cdot \mathbf{e}_k^{j\mu}. \quad (8)$$

The coefficients in (8) provide the displacement magnitudes along the direction of a given base vector and act as an order parameter, see Landau (1937) or Landau & Lifschitz (1971). The base vector necessarily exhibits the symmetry that results after displacement.

Analysis of the structural difference between phases II and IV may be undertaken in three steps; in the first, the difference vectors, $\Delta\mathbf{x}$, between the positions in $I4/m$ and $I\bar{4}$ are calculated, using the coordinate system of $I4/m$. This step yields 32 $\Delta\mathbf{x}$ vectors over all independent positions in phase IV, see Table S2, with each position having dimensions three times its Wyckoff multiplicity in Table 8. In the second step, the corresponding displacement is calculated for each orbit in $I4/m$ from its irreducible representation. The third step is the projection of the appropriate displacement of each of the 32 difference vectors $\Delta\mathbf{x}$, see (8). Since the original $P4/n$ cell of phase IV contains twice as many atoms as $I4/m$ or $I\bar{1}$, the atoms of the second set are displaced by the vectors of the first set in the following analysis; however, a phase factor $\mathbf{e}^{-i\mathbf{kr}}$ with wavevector $\mathbf{k} = (\frac{1}{2}, \frac{1}{2}, 0)$ applies, corresponding to the M point in the Brillouin zone of the tetragonal body-centered lattice.

The analysis leads to three active representations with coefficients $a_k^{j\mu} \neq 0$ for shifts with A_{1g}, A_{1u} and E_g symmetry. Displacements with E_g symmetry are only found for Pb atoms. Displacements with A_{1g} and A_{1u} symmetry are also active for the Pb atoms in addition to Al atoms in the Wyckoff position 8(g) and all F atoms, except those in positions 2(a), 2(b) and 2(c).

13.3. Structure refinement by use of irreducible representations

The starting hypothesis for the structure of phase III|360–315 K| takes the representations given in §13.1 as the displacement directions affording minimal energy; it also assumes one or a combination of several such directions as leading to this phase from the idealized prototype structure in $I4/mcm$, but with a symmetry that initially is undetermined. The hypothesis has been tested in two different approaches using the program *SIMREF*2.6 (Maichle *et al.*, 1988; Ritter *et al.*, 1998), originally designed for profile refinement by the Rietveld method. The first approach starts with an idealized structure and calculates the displacement magnitudes along the direction of several previously calculated normal-mode base vectors (Ritter, 1999). The second performs conventional structure refinements, see §13.5.1.

The program has been adapted in the first approach to the group theoretical aspects of structural change given above. Beginning with an idealized structure of higher symmetry R_0, taken here as $I4/mcm$ for the model giving the calculated

diffraction pattern, *SIMREF*2.6 calculates the displacement magnitudes from the lattice constants of the Laue class of lower symmetry. In contrast to a classical powder refinement in which the structural parameters are restricted to a given space group, the structural parameters determined herein are derived from the atomic displacement magnitudes $a_k^{j\mu}$ under displacement fields $\mathbf{e}_k^{j\mu}$ with the symmetry of the $j\mu$ irreducible representation, see Table 8. The symmetry-adapted atomic displacements in Table S9 are the vector magnitudes for each representation.

All the $j\mu$ irreducible representations except for A_{1g} break the symmetry of R_0. Hence, each yields a space group R that is a subgroup of R_0, see Table 8. The parameter thus corresponds to the magnitude of perturbation from the idealized structure, leading to space groups having symmetry in common with that of the irreducible representations involved.

The simultaneous refinement of two X-ray sets and one neutron data set, starting with $I4/mcm$ symmetry, gives displacements with major amplitudes that have only E_g and B_{2g} symmetry. As noted in §13.1, the *only* symmetry common to both displacement fields is $I\bar{1}$, consistent with the results given in Table S9 and analysis in §13.2.

13.4. The $Pb_5Al_3F_{19}$ phase system and the structure of phase III at 320 K

The structure of ferroelastic phase III was independently predicted on the premise that its coordinates were likely to differ little from the average of the known coordinates in phases V, IV and II, as given for each atom in Table 4 under 'Av(excluding III)'. The predicted and the final coordinates obtained by Rietveld refinement are presented in Table S10. Normal probability analysis of the two sets of 78 variable coordinates results in the approximately linear Q_{exp}–Q_{norm} distribution in Fig. S2(*a*), with a slope of 0.96 (1) and an intercept of 0.09 (1), excluding the eight outliers (Abrahams & Keve, 1971*b*). Although the outliers x(Al2), y(F12), z(F19), z(F6), x(F5), x(F4), y(F11) and z(F3) may originate in departures from the initial premise, the generally linear Q_{norm} distribution supports its use. Uncertainties in the averaged set of coordinates are larger than in the Rietveld set but remain within the normal range, with joint standard uncertainties that are well estimated, *cf.* Ross *et al.* (2002). The atomic coordinates from §13.3 and those from Table 4 proved to be equally adequate in refinement, giving the results in §4.2. The coordinates were used later by Bravic *et al.* (2000) as a starting model that led to $R = 0.065$, based on a set of F_{obs} measured at 300 K from a single crystal with the composition $Pb_5Al_{2.96}Cr_{0.04}F_{19}$; at room temperature, the latter is isostructural with phase III of $Pb_5Al_3F_{19}$ but differs from it in detail, see §14 and Table S11.

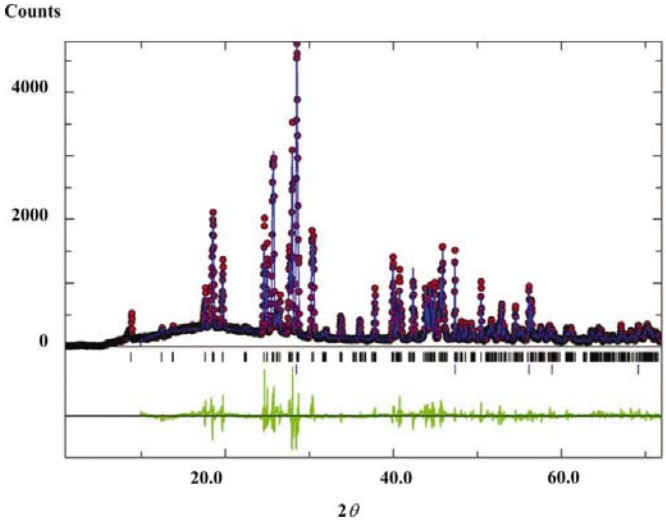

Figure 12
Red closed circles indicate the measured X-ray count rate (I/40 s), the black line their connected profile. The calculated intensity profile is given by the blue line and the reflection positions by the markers. The difference between experimental and calculated X-ray powder diffraction intensities for $Pb_5Al_3F_{19}$ phase III at 320 (2) K and counter 1 is given by the green line, see §13.5.

13.5. X-ray and neutron powder diffraction measurement

The X-ray powder patterns were recorded using a powder diffractometer in Guinier geometry (Ihringer *et al.*, 1994). The flat rotating sample was mounted within a cryostat equipped with a furnace that allows measurement over the thermal range $8 < T < 600$ K. Two scintillation counters, with angular separation $\Delta 2\theta = 20°$, simultaneously record the diffraction patterns with the respective angular ranges $1 < 2\theta < 72°$ and $22 < 2\theta < 93°$. The powder sample was maintained at 320 (2) K. The resulting phase III diffraction patterns, together with the calculated patterns and differences between them, are shown in Figs. 12 and 13. A monitor counter downstream of the Ge(111) oriented monochromator (Ihringer & Röttger, 1993, 1994) controls the stability of the monochromatic Cu $K\alpha_1$ primary beam.

The neutron diffraction data for phase III at 320 (2) K were recorded at the Berlin Neutron Scattering Center by means of

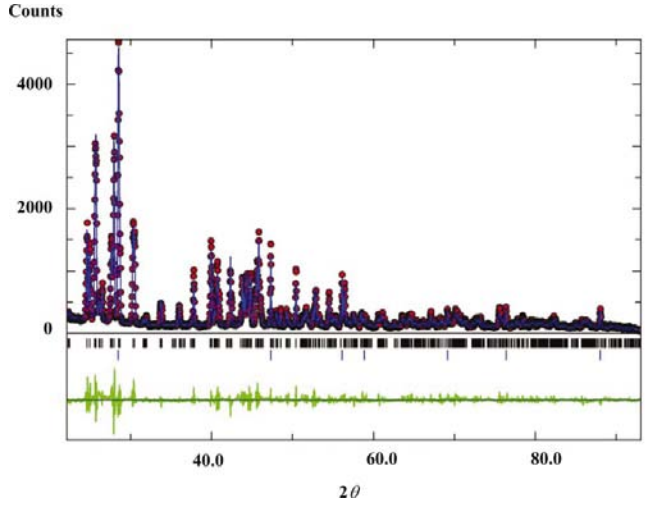

Figure 13
As in Fig. 12, but for the X-ray diffraction profiles of $Pb_5Al_3F_{19}$ phase III at 320 (2) K with counter 2, see §13.5.

Table 9
Experimental details for $Pb_5Al_3F_{19}$ phase III.

Crystal data	
Chemical formula	$Pb_5Al_3F_{19}$
Chemical formula weight	1477.91
Cell system	Triclinic
Space group	$I\bar{1}$
a (Å)	14.2622 (2)
b (Å)	14.2800 (2)
c (Å)	7.2340 (1)
α (°)	90.00 (1)
β (°)	90.510 (1)
γ (°)	90.00 (1)
V (Å^3)	1473.3 (2)
Z	4
D_m (Mg m^{-3})	6.66 (5) in phase IV
D_x (Mg m^{-3})	6.663 (1)
Radiation type	See §13.5
Wavelengths (Å)	1.54056 (Cu $K\alpha$), 1.226901 (neutron) λ
θ range (°) (Cu $K\alpha$ counters 1, 2)	0.93–71.92, 22.11–93.04
Neutron (°)	17.39–81.39
Temperature (K)	320 (2)
Data collection	
Diffractometer	See §6.4.1
Monochromator	X-rays, Ge(111); neutron, graphite
Sample container (Cu $K\alpha$; neutrons)	7 µm Kapton films, V can; He exchange gas
Instrument geometry	X-ray transmission, Guinier geometry; flat-cone, powder, multidetector
2θ step (°) (Cu $K\alpha_{1,2}$; neutrons)	0.025, 0.025, 0.4
θ_{max} (°) (X-ray 1; X-ray 2)	93.04; 81.39
Neutron	81.39
Refinement	
Background	Fifth-order polynomial
$R_{profile}$† (X-ray 1; X-ray 2; neutron; total)	0.114; 0.107; 0.045; 0.078
R_{exp}† (XR1; XR2; ND; total)	0.06; 0.06; 0.02; 0.049
R_{Bragg}† (XR1; XR2; ND; total)	0.085; 0.072; 0.081; 0.080
No. of parameters varied	145, including 82 structural
Full width at half-maximum (°) (min/max. XR1; XR2; ND)	0.115/0.315; 0.135/0.249; 0.298/0.965 at 75°
$(\Delta/\sigma)_{max}$	0.25
Refinement	
Computer programs	*SIMREF*26 (Ritter *et al.*, 1998)
Graphics programs	*ATOMS* (Dowty, 1999)

† $R_{profile} = \left(\sum_{i=1}^{N} |y_i^{obs} - y_i^{back} - y_i^{calc}|\right)/\left(\sum_{i=1}^{N} |y_i^{obs} - y_i^{back}|\right)$.

$R_{exp} = \left[(N-P)/\sum_{i=1}^{N}(y_i^{obs} - y_i^{back})^2\right]^{1/2}$.

$R_{Bragg} = \left(\sum_{k=1}^{K} |I_k^{obs} - I_k^{calc}|\right)/\left(\sum_{i=1}^{N} |I_k^{obs}|\right)$.

a flat-cone diffractometer, using the instrument E2/1 in the powder mode, and are shown in Fig. 14 together with the calculated profile (Neutron-Scattering Instrumentation at the Research Reactor BER II, 1996). A summary of the experimental details is given in Table 9.

13.5.1. Simultaneous Rietveld analysis of the X-ray and neutron powder diffraction profiles. The final structure of phase III in space group $I\bar{1}$ was determined by refining the known displacements along the normal modes, see §13.3, using *SIMREF*2.6 (Ritter *et al.*, 1998). The results agree with those obtained using the predicted starting model in §13.4, see also Table S10. Three data sets consisting of two high-resolution X-ray and one neutron powder pattern, measured as in §13.5, were refined simultaneously. The program calibrated the 2θ scale in each set by means of a third-order polynomial that best fits the lines of a standard material (Si, NBS Standard Reference Material 640*b*) mixed with the sample. The experimental temperature of 320 (2) K was estimated by the use of the appropriate thermal expansion coefficient for Si (Okada & Tokumaru, 1984; Lyon *et al.*, 1977).

Least-squares convergence was slow, with the standard uncertainties in y [s.u.(y)] increasing sharply if all 78 x, y and z parameters were varied simultaneously. A total of 75 unconstrained atomic position coordinates together with the 11 isotropic thermal/static atomic displacement parameters (ADPs) were hence varied in the final refinements, holding Pb2(x,y,z) invariant after the condition $\Delta\xi_{max}$/s.u. $\leq$ 0.05 (where $\Delta\xi$ is the difference in successive ξ values) had been reached. The Al atoms were assigned a common ADP value, as were all F atoms in the same octahedron except for ADP(F13 and F14) in $Al3F_6$, which were assigned a value that could differ from that reached by ADP(F15, F16, F17 and F18); the non-octahedral F19 and F20 atoms were also assigned a common ADP value. The results are given in Table 3 and the CIF, with magnitudes and s.u.'s for the Pb2 variable parameters from the preceding refinement cycle. The structure is shown in Figs. 5 and 6.

14. Crystal structures of $Pb_5Al_{2.96}Cr_{0.04}F_{19}$ at 300 K and $Pb_5Cr_3F_{19}$ phase II

14.1. Comparison of $Pb_5Al_{2.96}Cr_{0.04}F_{19}$ at 300 K and $Pb_5Al_3F_{19}$ phase III

The structure of non-stoichiometric $Pb_5Al_{2.96}Cr_{0.04}F_{19}$ at 300 K, refined in the space group $P\bar{1}$ by Bravic *et al.* (2000), is comparable to that of $Pb_5Al_3F_{19}$ in phase III. The atomic coordinates reported for $Pb_5Al_{2.96}Cr_{0.04}F_{19}$ are listed in

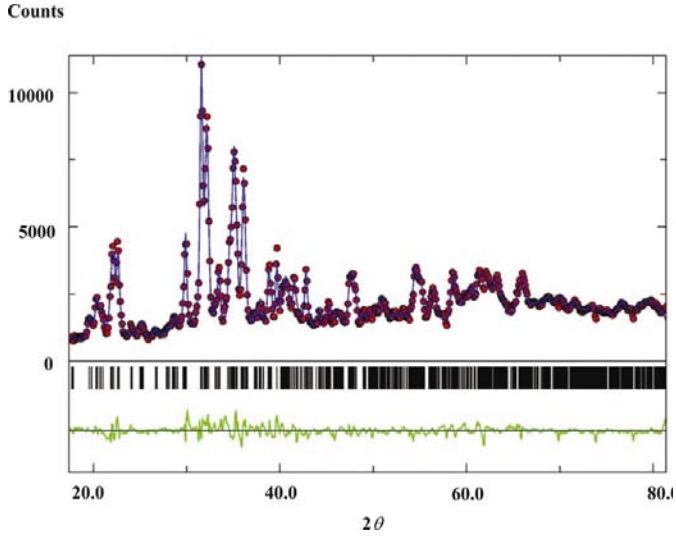

Figure 14
As in Fig. 12, but with the closed red circles giving the total number of neutrons (I/6 h) at each point on the neutron diffraction profile of $Pb_5Al_3F_{19}$ phase III at 320 (2) K, see §13.5.

Table S11 following the transformation given in (9) to a setting in space group $I\bar{1}$ that allows comparison with the coordinates in all other phases of $Pb_5Al_3F_{19}$:

$$x = (x' + y')/2;\ \ y = (-x' + y')/2;\ \ z = -(x' + y')/2 + z', \tag{9}$$

where the primed coordinates are as given in the primitive unit cell. Differences between atomic coordinates derived from Bravic *et al.*'s (2000) $(x_B,y_B,z_B)_{300\ K}$ values and the Rietveld analysis $(x_{RA},y_{RA},z_{RA})_{320\ K}$ results in Table 3 are given in Table S11, together with the joint standard uncertainties.

The analysis of Q_{exp}–Q_{norm} (Abrahams & Keve, 1971*b*) shows that all the experimental deviates from these two studies are distributed close to normal, except for *y*(Pb5), *z*(Pb2), *x*(Pb5), *y*(Pb4) and *y*(Pb4), in order of decreasing magnitude, see Fig. S2(*b*). Excluding these five outliers, the slope for all the remaining deviates is 11.29 (18) with an intercept of −1.6 (2), as determined by linear regression with respect to a normal distribution. In the absence of systematic error, the average joint s.u. in Q_{exp} may be taken as underestimated by a factor of 11.29. However, this factor significantly exceeds that derived from the Q_{exp}–Q_{norm} analysis in §13.4 based on the phase III Rietveld refinement and the $Pb_5Al_3F_{19}$ phase system deviates; it is similarly in excess of the general range within which s.u.'s are underestimated, *viz.* $\lesssim 2$. The magnitude of the underestimate is indicative of the systematic differences between the two structures. The largest difference between the corresponding final atomic coordinates is 0.522 (16) Å for Pb5, with nine others larger than 10σ that include 0.50 (3) Å for F6, 0.45 (3) Å for F10 and 0.40 (3) Å for F11, see Table S11. The structure of pure $Pb_5Al_3F_{19}$ at 320 K hence differs from that of $Pb_5Al_{2.96}Cr_{0.04}F_{19}$ at 300 K with high significance, leading to the significant decrease in $T_{IV,III}$ observed on replacing minor proportions of Al by a 3*d* element, see §12.

14.2. Comparison of $Pb_5Cr_3F_{19}$ phase II and $Pb_5Al_3F_{19}$ phase V

The significant differences between $Pb_5Al_{2.96}Cr_{0.04}F_{19}$ at 300 K and $Pb_5Al_3F_{19}$ phase III at 320 K, see §14.1, led to an investigation of the possible differences between the structures of $Pb_5Cr_3F_{19}$ phase II (Abrahams *et al.*, 1990) and $Pb_5Al_3F_{19}$ phase V (Sarraute *et al.*, 1996) by Q_{exp}–Q_{norm} analysis. The results given in Fig. S1(*c*) reveal that all but four Q_{exp} terms vary rather linearly with Q_{norm} for a slope of 3.33 (4) and zero intercept; the remaining terms approach linearity, barely exceeding the bounds expected for negligible systematic error with a joint standard uncertainty underestimated by a factor of 3.33. The four outliers $Q_{exp}[z(Pb2)]$ = 18.50, $Q_{exp}[y(Pb1)]$ = 10.74, $Q_{exp}[z(F2)]$ = 9.18 and $Q_{exp}[z(Al1,Cr1)]$ = 6.60 are, however, highly significant with differences ranging from 0.17 (2) to 0.06 (2) Å in one or more coordinates. Full replacement of Al by Cr with its 3*d* electrons hence has a highly significant influence on the structure of $Pb_5Al_3F_{19}$ phase V, although the influence is smaller than in the less stable phase III.

The results in §14.1 unambiguously demonstrate that while the structure of $Pb_5Al_{2.96}Cr_{0.04}F_{19}$ at 300 K resembles $Pb_5Al_3F_{19}$ phase III at 320 K, as the structure of $Pb_5Cr_3F_{19}$ at 300 K resembles $Pb_5Al_3F_{19}$ phase V at 160 K, each pair of structures nevertheless exhibits significant differences.

The minima in the $Pb_5Al_3F_{19}$ free-energy surface, see §12, giving rise to four phase transitions with the concomitant formation of two different ferroic properties, are unique among fluorides that have been investigated previously. Several oxides exhibit a comparable or larger number of phase transitions accompanied by the formation of ferroic properties, with six transitions reported in $NaNbO_3$ and WO_3, and four in $BaTiO_3$ and several members of the boracite family, including $Fe_3B_7O_{13}Cl$.

It is a pleasure to thank Vero Andriamampianina and Sabine Sarraute for sample preparation, and also the latter for preliminary diffraction studies on phase III. Thanks are also proffered to Louis Rabardel and Dominique Denux for calorimetric measurements, and D. Hohlwein for assistance at the neutron powder diffractometer in Berlin, the Alexander von Humboldt Foundation for an extension of the Humboldt Prize to one of us (SCA) during which this work was begun, the National Science Foundation (DMR-9708246, DMR-0137323), the Deutsche Forschungsgemeinschaft (project Ih 9/3-4) and the Bundesministerium für Bildung und Forschung for financial support. Comments on the manuscript by Professors Jinzo Kobayashi, Jean-Claude Tolédano and Robert Hatt are warmly appreciated. Discussions with Professor I. David Brown contributed notably to the clarity of this paper and are also gratefully acknowledged.

References

Abrahams, S. C. (1979). *God. Jugo. Centra Kristallogr.* **14**, 1–12.
Abrahams, S. C. (1988). *Acta Cryst.* B**44**, 585–595.
Abrahams, S. C. (1994). *Acta Cryst.* A**50**, 658–685.
Abrahams, S. C., Albertsson, J., Svensson, C. & Ravez, J. (1990). *Acta Cryst.* B**46**, 497–502.
Abrahams, S. C. & Keve, E. T. (1971*a*). *Ferroelectrics*, **2**, 129–154.
Abrahams, S. C. & Keve, E. T. (1971*b*). *Acta Cryst.* A**27**, 157–165.
Abrahams, S. C., Kurtz, S. K. & Jamieson, P. B. (1968). *Phys. Rev.* **172**, 551–553.
Aizu, K. (1970). *Phys. Rev. B*, **2**, 754–772.
Andriamampianina, V. (1992). Thèse de Docteur, L'Université Bordeaux I.
Andriamampianina, V., Gravereau, P., Ravez, J. & Abrahams, S. C. (1994). *Acta Cryst.* B**50**, 135–141.
Aroyo, M. I. & Perez-Mato, J. M. (1998). *Acta Cryst.* A**54**, 19–30.
Arquis-Canouet, S., Ravez, J. & Abrahams, S. C. (1986). *J. Appl. Cryst.* **19**, 374–376.
Bravic, G., von der Mühll, R. & Ravez, J. (2000). *J. Solid. State Chem.* **155**, 427–432.
Brese, N. E. & O'Keefe, M. (1991). *Acta Cryst.* B**47**, 192–197.
Dowty, E. (1999). *Atoms*, Version 5.0. Shape Software, Kingsport, TN 37663. http://www.shapesoftware.com.
Glazer, A. M. (1972). *Acta Cryst.* B**28**, 3384–3392.
Ihringer, J. & Abrahams, S. C. (1984). *Phys. Rev. B*, **30**, 6540–6548.

Ihringer, J., Ravez, J. & Abrahams, S. C. (1994). *Z. Kristallogr.* **209**, 853–857.
Ihringer, J. & Röttger, K. (1993). *J. Phys. D*, **26**, A32–A34.
Ihringer, J. & Röttger, K. (1994). *J. Appl. Cryst.* **27**, 1063–1065.
Ischuk, V. M. (2001). *Ferroelectrics*, **255**, 73–109.
Krivovichev, S. V. & Filatov, S. K. (1999). *Acta Cryst.* B**55**, 664–676.
Landau, L. D. (1937). *Phys. Z. Sowjetunion*, **11**, 26–47.
Landau, L. D. & Lifschitz, E. M. (1971). *Lehrbuch der Theoretischen Physik, Band V, Statistische Physik*. Berlin: Akademie-Verlag.
Lyon, K. G., Salinger, G. L. & Swenson, C. A. (1977). *J. Appl. Phys.* **48**, 865–868.
Maichle, J. K., Ihringer, J. & Prandl, W. (1988). *J. Appl. Cryst.* **21**, 22–27.
Mentzen, B. F. & Latrach, A. (1983). *J. Appl. Cryst.* **16**, 430.
Neutron-Scattering Instrumentation at the Research Reactor BER II (1996). BENSC, Glienicker Strasse 100, D 14109 Berlin, 12–13.
Okada, Y. & Tokumaru, Y. (1984). *J. Appl. Phys.* **56**, 314–320.
Omari, M. E., Réau, J.-M., Sénégas, J., Ravez, J., Abrahams, S. C., Nadiri, A. & Yacoubi, A. (1998). *J. Chem. Phys.* **108**, 2896–2902.
Ravez, J. & Abrahams, S. C. (1998). *C. R. Séances Acad. Sci.* **1**, IIc, 15–19.
Ravez, J., Andriamampianina, V., Simon, A., Grannec, J. & Abrahams, S. C. (1991). *J. Appl. Phys.* **70**, 1331–1336.
Ravez, J., Andriamampianina, V., Simon, A., Rabardel, L., Ihringer, J. & Abrahams, S. C. (1994). *J. Appl. Cryst.* **27**, 362–368.
Ravez, J., Simon, A., Andriamampianina, V., Grannec, J., Hagenmuller, P. & Abrahams, S. C. (1990). *J. Appl. Phys.* **68**, 3529–3531.
Ritter, H. (1999). Unpublished.
Ritter, H., Ihringer, J., Maichle, J. K. & Prandl, W. (1998). *SIMREF*26, http://www.uni-tuebingen.de/uni/pki/simref/simref.html.
Ross, C. R., Bauer, M. R., Nielson, R. M. & Abrahams, S. C. (2002). *Acta Cryst.* B**58**, 841–848.
Sarraute, S., Ravez, J., Bravic, G., Chasseau, D. & Abrahams, S. C. (1995). *Acta Cryst.* C**51**, 1731–1732.
Sarraute, S., Ravez, J., von der Mühll, R., Bravic, G., Feigelson, R. S. & Abrahams, S. C. (1996). *Acta Cryst.* B**52**, 72–77.
Shannon, R. D. (1976). *Acta Cryst.* A**32**, 751–767.
Stokes, H. T. & Hatch D. M. (1988). *Isotropy Subgroups of the 230 Crystallographic Space Groups*. Singapore: World Scientific Publishing Co.
Tolédano, J.-C., Glazer, A. M., Hahn, Th., Parthé, E., Roth, R. S., Berry, R. S., Metselaar, R. & Abrahams, S. C. (1998). *Acta Cryst.* A**54**, 1028–1033.
Tolédano, J.-C. & Tolédano, P. (1987). *The Landau Theory of Phase Transitions*. Singapore: World Scientific Publishing Co.
Wadhawan, V. K. (2000). *Introduction to Ferroic Materials*. Amsterdam: Gordon and Breach.
Wang, J., Neaton, J. B., Zheng, H., Nagarajan, V., Ogale, S. B., Liu, B., Viehland, D., Vaithyanathan, V., Schlom, D. G., Waghmare, U. V., Spaldin, N. A., Rabe, K. M., Wuttig, M. & Ramesh, R. (2003). *Science*, **299**, 1719–1722.